Method for Comparing Porous Carbon Electrode Performance in Redox Flow Batteries

Journal of The Electrochemical Society, 2020 **167** 110542
1945-7111/2020/167(11)/110542/15/$40.00 © 2020 The Electrochemical Society ("ECS"). Published on behalf of ECS by IOP Publishing Limited

Method for Comparing Porous Carbon Electrode Performance in Redox Flow Batteries

Andrew A. Wong[a] and **Michael J. Aziz**[*,z]

Harvard John A. Paulson School of Engineering and Applied Sciences, Cambridge, Massachusetts 02138, United States of America

We present a method for comparing porous electrodes for use in redox flow batteries. By comparing physical and electrochemical properties of six carbon cloth electrodes (CCEs) including hydraulic permeability, Ohmic resistance, and mass transport overpotential, we show how optimal engineering conditions such as compression and electrolyte flow rates can be derived. These results are combined and applied to a quinone-based redox flow battery, leading to a peak power density around 0.4 W cm^{-2} for several different CCEs. This method can be applied broadly to other electrode architectures and flow battery chemistries, and provides a comprehensive framework for their comparison.
 [DOI: 10.1149/1945-7111/aba54d]

Manuscript submitted May 15, 2020; revised manuscript received July 3, 2020. Published July 21, 2020.

Supplementary material for this article is available online

List of Symbol

A	cross-sectional flow area [m^2]
ASR_{ohmic}	electrode Ohmic area specific resistance [Ωcm^2]
ASR_{pump}	effective hydraulic area specific resistance from pumping [Ωcm^2]
β	fitting parameter [1]
c	capacity-limiting electrolyte concentration [mol l^{-1}]
Δc	change in capacity-limiting electrolyte concentration [mol l^{-1}]
E	Young's elastic modulus [Pa]
$E^{0'}$	formal potential [V]
ε_t	true strain [1]
ε	engineering strain [1]
F	Faraday's constant [94685 C mol^{-1}]
i	electronic current density [A cm^{-2}]
K_{TP}	through-plane fluid permeability [m^2]
$K(t)$	fluid permeability (as a function of compressed stack thickness) [m^2]
μ	reference dynamic viscosity [mPa·s]
μ'	variable electrolyte viscosity [mPa·s]
n	number of transferrable electrons per molecule of reactant [1]
η_{MT}	mass transport overpotential [V]
[O]	oxidized species concentration [mol l^{-1} mol l^{-1}]
ΔP	pressure drop [Pa]
$\dot{Q}$	volumetric fluid flow rate [L s^{-1}]
R	universal gas constant [8.314 J mol^{-1} K^{-1}]
[R]	reduced species concentration [mol l^{-1}]
r_{in}	inlet radius [m]
r_e	Exit radius [m]
S	pump efficiency scaling factor [1]
σ	compressive stress [Pa]
t	compressed stack thickness [m]
t_0	uncompressed stack thickness [m]
U	electrolyte utilization (conversion per pass) [1]
U^*	mass transport limited electrolyte utilization [1]
ΔVE_{pump}	effective voltage efficiency loss from pumping [1]
V_{OC}	full cell open circuit voltage [V]
W_C	flow field channel width [m]
W_L	flow field landing width [m]
ψ_{pump}	fluid pump efficiency [1]

*Electrochemical Society Member.
[a]Present Address: Lawrence Livermore National Lab, Livermore, California, 94550, USA.
[z]E-mail: maziz@harvard.edu

Porous materials consisting of felts, papers, and cloths have been widely used as electrodes in redox flow batteries (RFBs)[1] and fuel cells.[2] While porous electrodes composed of metals such as copper (Cu) and nickel (Ni),[3] and metal oxides such as tin oxide (SnO_2) and cobalt oxide (Co_3O_4)[4] have been used for these applications, electrically conductive porous carbon electrodes can be inexpensive alternatives that exhibit high surface area, allow for fine feature sizes, are resistive to corrosion, have high oxygen and hydrogen evolution reaction overpotentials, and can be substantially compressed without brittle failure.[5,6] Several different processing methods, such as roll-to-roll fabrication, exist to produce porous carbon electrodes with varying degrees of complexity.[7] However, these methods often lack precise control of mesoscale properties such as pore size and void distribution, leading to poor mass transport behavior.[8]

Woven carbon cloth electrodes (CCE) have recently been explored as porous electrodes for battery applications due to their dual length scale features;[9,10] in RFBs, this opens opportunities for potentially lower mass transport overpotentials.[11] Often CCEs consist of a woven assembly of fiber bundles, allowing for advection-dominated mass transport between the bundle weaves, and diffusion-dominated mass transport within the bundles themselves.[11] CCEs do not require binder additives to hold their shape, facilitate anisotropic (directional) fluid flow, and can increase the stacking density of carbon fibers allowing for higher per-volume surface area.[12] These materials can be manufactured using modern textile weaving machines, enabling precise control over the warp and weft spacing, thread count, and fabric thickness, and allowing for custom patterns. Furthermore, the ability to adjust the weave pattern on the fly opens unique opportunities for rapid iteration and flexible batch sizes, supporting the pursuit of an optimal electrode structure.[10,13]

In order to establish the potential of using woven CCEs for electrochemical applications, it is important to create a framework for evaluating these materials for a given use case. In this work we explore the physical and electrochemical properties of six commercial woven CCEs used for a quinone-ferrocyanide redox flow battery (RFB). We analyze the permeability, electrical conductivity, and electrochemical properties of these CCEs. Mass transport overpotential is measured by utilizing an electrolyte-limited symmetric cell and subtracting the DC full-cell resistance. The results for a variety of flow rates collapse to a mass transport limited utilization (percent electrolyte conversion per pass) that can be approximated by a simple Nernstian analytical expression. Combining all of these results, we create a pumping-corrected voltage efficiency map under a range of operating conditions and identify the components most

significantly limiting the full cell performance. The procedure can be amenable to other porous electrode materials and provides insights into design optimizations for woven CCEs.

Experimental

Six carbon cloth electrodes were used for this study and are pictured in Fig. 1.

(a) Clean Fuel Cell Energy, LCC Carbon Cloth B-1 Designation A (CFCE),
(b) Elat® Hydrophilic Plain Cloth (Elat),
(c) Engineered Fibers Technology, LCC SpectraCarb™ 2225 Type 900 (Spectracarb),
(d) Toray Group Zoltek™ PX35 Plain Weave (Zoltek),
(e) AvCarb® 1186HCBA (HCBA),
(f) AvCarb® 1698NHCBA (NHCBA)

Several of the CCEs were largely hydrophobic as received; to make the electrodes hydrophilic, each was treated in an oxygen plasma chamber (Technics 220) at 10 SCCM/min O_2 flow, 75 mW for 5 min. Prior research has demonstrated that carbon treatment by oxygen plasma increases the surface density of polar carbon-oxygen groups without changing the Brunauer–Emmett–Teller (BET) surface area.[14] BET surface area was measured before and after oxygen plasma treatment (Micromeritics 3Flex). For the BET measurements, CCEs samples were coarsely cut and weigh to ~0.2 g. Samples were then degassed and dehydrated under vacuum for >12 h while externally heated to 200 °C. Post-dehydration mass could fluctuate by up to 30 mg. The samples were then re-evacuated, submerged in liquid nitrogen alongside a reference port, and anhydrous nitrogen was slowly added to the samples. Below 0.1 P/P_0 and above 0.98 P/P_0 relative pressure, data are measured in dose increments of ~0.5 cm^3 STP to characterize the ultrafine and coarse nanoporous surface structures respectively. Between 0.1 P/P_0 and 0.98 P/P_0, data are measured in increments of 0.05 P/P_0. Both forward and reverse scans were performed to verify no hysteresis indicative of an imperfect vacuum seal. Surface functionalization was measured by X-ray photoelectron spectroscopy (XPS, Thermo Scientific K-Alpha+) also before and after treatment. XPS was performed at $<8 \times 10^{-8}$ mBar (<8 mPa) pressure. Flood gun spot size was 50 μm with 5 μm raster steps averaged over a 200 μm × 200 μm area centered on the weave apex to minimize background interference. Rigorous pretreatment studies on porous carbon electrodes have been published[15] and the impact of oxygen functional groups[16] and aging are ongoing areas of research. However, on the timescale of the experiments described in this work, we measure minimal changes in performance between measurement.

Micrographs of each electrode were collected with a scanning electron microscope (SEM, Zeiss Ultra Plus). The electrode thickness was measured by a dial thickness gage by placing a 2.5 cm diameter sample under a glass slide with a total force of 0.5 N (1 kPa uniaxial compressive stress). The subsequent calculations of engineering strain use these measured thickness values.

Electrode stress-strain characteristics were measured with an Instron® 3369 mechanical testing machine and are corrected with a stress-strain profile measured without a sample present to account for compression of the Instron® mount. The measured load is converted to stress by dividing the geometric area of the electrode. The maximum compression on the electrode is ultimately limited by the design of the fully assembled cell and is constrained by a maximum load on the cell. The full- and symmetric-cell experiments described later in this work both use 9 in^2 graphite flow plates compressed between aluminum end plates using six 3/8"−24 bolts tightened to 90 inch-lbs. torque. Under these conditions the load applied per bolt is approximately 1200 lbs. (~5300 N), resulting in a total compressive stress of 5.5×10^6 Pa over the complete cell area when assembled. This provides an upper limit on the compressive stress, and thereby on the strain, experienced by the CCEs with the cell used in these experiments.

The electrical conductivity and fluid permeability of each electrode were measured as functions of strain using a custom

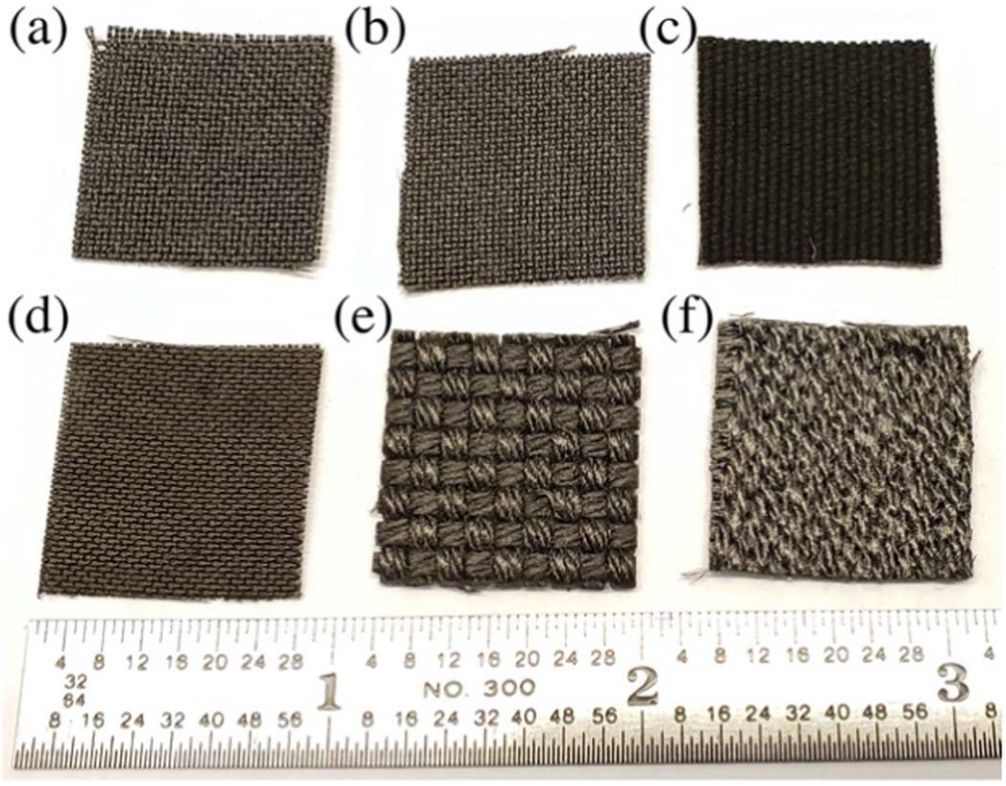

Figure 1. Photograph of the six carbon cloth electrodes used in this study: (a) CFCE), (b) Elat, (c) Spectracarb, (d) Zoltek, (e) HCBA, (f) NHCBA. Each is cut to 5 cm^2 for use in a symmetric- and full-cell configuration.

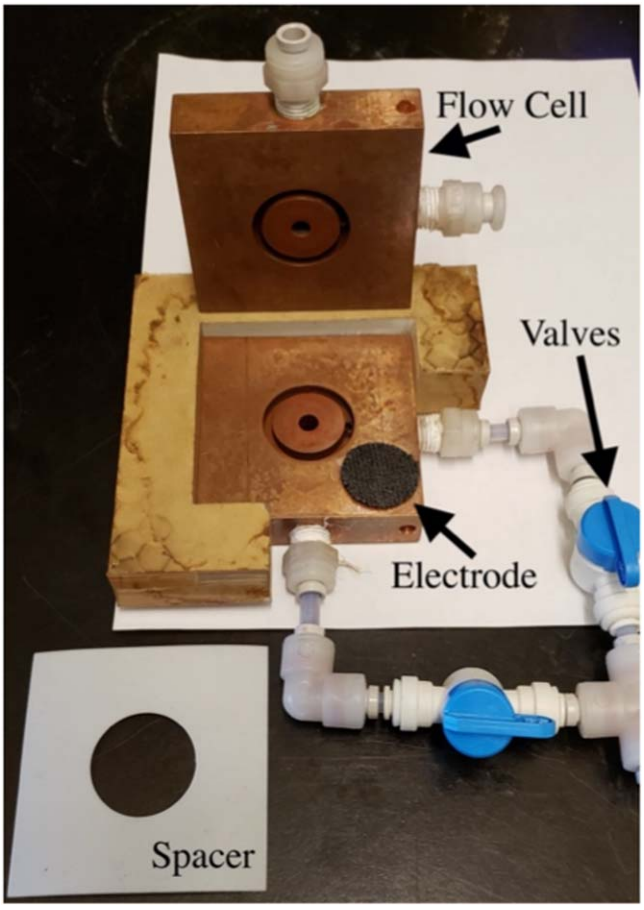

Figure 2. Photograph of the combined permeability and resistivity cell made from machined copper. A 1-inch diameter electrode is centered on the flow cell, and the PTFE shims define the thickness around the electrode. Through-plane permeability measurements are performed with flow from one center hole, through the compressed electrode, and out through the opposing center hole. In-plane permeability measurements are performed with flow from one center hole, radially out through the electrode, and finally exiting through the circular trench. External valves control the flow direction.

designed cell pictured Fig. 2, and also described in previous work.[17] This cell uses PTFE shims to achieve a desired compressed thickness and can be used to measure in-plane and through-plane fluid permeability, and through-plane electrical conductivity sequentially. Circular electrodes, pretreated by oxygen plasma and cut to one-inch diameter, were stacked between the two mirroring copper plates consisting of a 0.25-inch diameter center hole and a one-inch inner diameter circular trench. The setup was compressed by several squeeze action C-clamps and we assume no elastic or plastic deformation of the PTFE spacers. Deionized water (~1 mPa·s at 20 °C) was circulated by a gear pump and directed through the cell via a series of external valves. Fluid flow rates and pressures were measured at the cell inlet, with the exit emptying into an open-air reservoir. For the through-plane measurements, water passed through the electrode via the opposing center holes. For the in-plane measurements, water entered through one center hole, flowed radially through the electrode stack, and exited through the circular trenches surrounding the sample.

Mass transport was first characterized by using a symmetric-cell configuration described by Gerhardt et al.[17] with a common reservoir of potassium ferri/ferrocyanide (0.1 M $K_4Fe(CN)_6$, 0.01 M $K_3Fe(CN)_6$, 1.0 M KCl, 0.01 M KOH) independently pumped to the cathode and anode at the same volumetric flow rate. A potentiostat (Gamry 3000 and Reference 30k booster) was used for electrochemical characterization, including electrochemical impedance spectroscopy (EIS), linear sweep voltammetry (CV), and chronoamperometry (CA), to measure the cell polarization. A flow-through flow plate (Fig. S1a is available online at stacks.iop.org/JES/167/110542/mmedia) was used to capture the mass transport limited regime; each experiment is run at flow rates ranging from 20 to 100 ml min^{-1} using a peristaltic pump.

Full-cell polarization curves were obtained with a negolyte composed of 4,4'-((9,10-anthraquinone-2,6-diyl)dioxy)dibutyrate ($DBEAQ^{2-}$/DBEAQ), 0.5 M K_2DBEAQ in 0.01 M KOH, against a posolyte composed of 0.5 M $K_4Fe(CN)_6$ and 0.05 M $K_3Fe(CN)_6$ in 0.01 M KOH (all at pH 12). This chemistry has been previously reported as having record-setting capacity retention rate[18] but could benefit from an increase in power density. For these full cell measurements, we use a Fumatech E620K cation conducting membrane to match the conditions of the previous report. A custom interdigitated flow field (IDFF) geometry (Fig. S1b) was previously reported to be an optimal geometry for a similar electrolyte composition,[17] and is used for the full cell measurements.

This method for evaluating CCEs, and by extension other porous electrodes, incorporates three distinct components:

(1) We measure the in-plane and through-plane permeabilities and conductivities of the electrode as functions of compressive strain. The lower strain limit is defined by the uncompressed thickness of the electrode; the upper strain limit is physically defined by the point of zero permeability but is pragmatically dependent on the minimum acceptable permeability (highest acceptable pressure drop) for a given application. These limits can be used to establish a range of compressions that are acceptable for a particular application and guide toward a compression that gives a minimum effective area specific resistance (ASR). A description on calculating an effective ASR is detailed in the Results and Discussion section.

(2) We measure the mass transport and charge transfer resistances of a compressed electrode in a symmetric-cell configuration as a function of volumetric flow rate using a representative electrolyte. In this work, we compress each electrode to match the strain that enables a minimum effective ASR at an electrolyte utilization (single pass conversion efficiency) of 3%–5% to demonstrate this method. Other applications may wish to explore a range of compressive strains for a single electrode or target higher or lower electrolyte utilization fractions.

(3) Using the insights gained from the first two sets of measurements, we measure the polarization performance of a full cell as a function of state of charge (SOC). Though this measurement is again amenable to trial under a range of electrode compressions

Table I. CCE physical characteristics. Electrode thickness measured by a dial thickness gauge. Filament diameter measured from SEM micrographs. Weave periodicity measured from both SEM micrographs and optical micrographs.

Electrode	CFCE	Elat	Spectracarb	Zoltek	HCBA	NHCBA
Thickness (μm)	560	470	670	520	1650	1250
Variation (μm)	±25	±15	±15	±25	±40	±50
Filament diameter (μm)	8	8	10	8	9	9
Variation (μm)	±1	±1	±2	±2	±1	±1
Weave periodicity (cm^{-1})	20	20	18	17	4	n/a

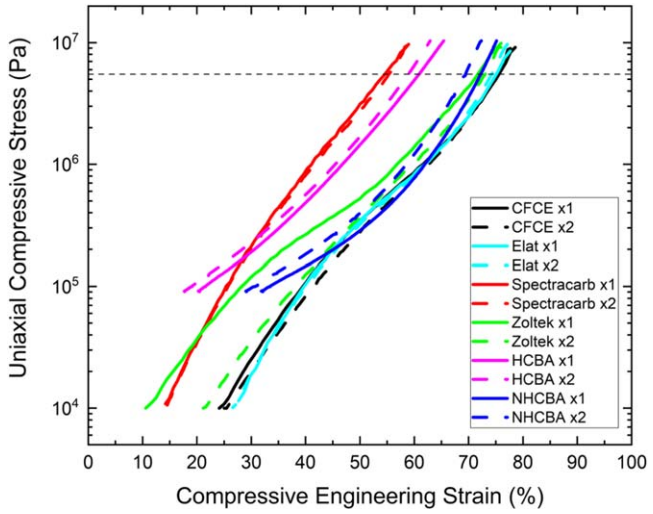

Figure 3. Semi-log plot of uniaxial compressive stress vs. strain. A nearly exponential relationship is observed for all electrodes tested. The compressive stress estimated for the assembled cell stack is 5.5×10^6 Pa, creating an upper limit to practical compressive stresses.

and electrolyte volumetric flow rate, the aim of this work is to circumvent a parametric multi-variable study by providing a systematic method to compare porous electrodes in electrochemical applications.

Results and Discussion

Table I shows the electrode thickness measurements, which are used for all subsequent strain calculations. The electrodes exhibit a wide range of thicknesses compared to one another and are all significantly greater than most carbon paper electrodes (e.g. SGL 39AA is 280 μm). This difference may provide future opportunities for manufacturing optimization of uncompressed electrode thickness.

A compressive stress-strain relationship (Fig. 3) was measured with the Instron®, setup in compression mode. The trend shows a nearly exponentially increasing compressive stress (σ) as a function of engineering strain, which deviates from a simple linear relationship expected from Hooke's Law ($\sigma = E\varepsilon_t$) for many solids, where E is the Young's Elastic Modulus and ε_t is the true strain. This exponential relationship between compressive stress and strain in random fiber networks has been previously reported, stemming from the relationship between true strain and fiber density.[19] Both single and double electrode layers were measured to identify trends in interlayer overlap. All single and double layer experiments exhibit a tightly correlated relationship except for Zoltek, which shows a small 10% difference in strain at low compressive stresses. Because the weaves disrupt the planarity of the CCEs, it is plausible to have stacked electrodes exhibit slightly shifted stress-strain behavior if the weaves deviate in alignment.

As described in the Experimental section, the compressive stress applied to the flow field plate is 5.5×10^6 Pa, which provides an upper bound for the maximum practical compressive stress on the electrode with this particular cell configuration. If the electrode were to experience a stress greater than the stress applied to the flow field plate, fluid would leak around the gaskets. For most of the electrodes, 5.5×10^6 Pa allows for a maximum of 50%–70% strain —a value that will later become a factor for accessing an optimum electrode compressed thickness.

To capture the underlying electrode surface topography and morphology, samples were observed with an SEM (Fig. 4). These micrographs are used to determine the carbon wire filament diameter and weave periodicity also reported in Table I. All samples exhibited nearly symmetric periodicity in both the warp and weft directions, except for NHCBA whose underlying structure was difficult to ascertain (see Fig. 1). Note that periodicity is measured while the electrodes are uncompressed, whereas unconstrained compression may cause the weaves to splay, decreasing the true periodicity when assembled in a full cell. Future architectures could employ asymmetric periodicity for tailored performance, achieving a preferential fluid flow direction. Also observed in the SEM micrographs, CFCE, Elat, and Zoltek electrodes exhibit a single fiber bundle in each weave, which all can lay topologically flat. Spectracarb in contrast has three-braid fiber bundles, which are woven together. The two AvCarb electrodes also have three-braid fiber bundles, but each of the braids is twisted, creating a complex multi-length scale structure. Though the fiber diameters are relatively similar, these AvCarb bundle braids have a significantly larger diameter, leading to a smaller weave periodicity. Full details on the weave architecture may need to incorporate a deeper understanding of the CCE manufacturing process.

BET and XPS were used to characterize the electrode surface area and elemental composition respectively, both as received and after oxygen plasma treatment. As can be seen in Fig. 5, the BET surface area does not change appreciably after oxygen plasma treatment, a result consistent with those previously reported.[14] Slight differences in total adsorbed molecules (typically $<10\%$) are attributed to sample variation rather than pretreatment, as determined by several repeated runs. Interestingly, all samples except for Spectracarb exhibit nearly linear absorption as a function of partial pressure and nearly identical quantities of total adsorbed molecules, indicative of smooth filament surfaces and comparable surface to mass ratios. This suggests that the filaments are fully dense without nanoscale surface roughness. The Spectracarb, in contrast, shows very large molecule absorption at low partial pressures, suggesting these filaments have substantial nanoscale surface features that enhance the microporous surface area. Some reports suggest that high active surface area is an advantage for electrochemical systems due to a reduction in charge transfer resistance;[20] however, as will be seen shortly, this particular electrode exhibits physical and electrical properties that lead to poor performance.

Full spectrum XPS results can be found in Fig. 6. All samples exhibit strong carbon and oxygen peaks, with the surface oxygen peak increasing after the oxygen plasma treatment. Several additional peaks including sulfur (S), nitrogen (N) and silicon (Si) are noted when applicable. With the exception of the ~13 at% Si peak in the Zoltek samples, all other additional peaks are <2 at%. This study will not explore the effect of these trace element additives, but we report these findings should they become relevant for future studies. Other studies, for example, have found the addition of boron (B) to carbon enhances the catalytic activity of RFB electrodes.[21] High resolution scans of the oxygen peak (Fig. S2) show equal or increased oxygen content after the oxygen plasma treatment for all electrodes.

Figure 7 zooms in on the XPS spectra to show the carbon peak in high resolution. The post-treatment Spectracarb spectrum in panel (c) has by far the greatest shift toward carbon-oxygen bonds, likely due to the high surface area (measured by BET in Fig. 5) accessible to the oxygen plasma. Figure 7(g) deconvolutes the spectrum for the Spectracarb electrode after oxygen plasma into the contributions from the C–C/C–H, O–C–O, O–C=O, and π-π bonds. The results of the deconvolution of the various panels support the findings observed from Figs. 6 and S2, demonstrating a post-treatment increase in carbon-oxygen bonds, resulting in a hydrophilic electrode surface.

The custom cell depicted in Fig. 2 was used to measure in-plane and through-plane permeability of each electrode as functions of strain as shown in Fig. 8, following a similar procedure to Feser et al.[22] Through-plane permeability (K_{TP} [m^2]) was calculated by Darcy's Law

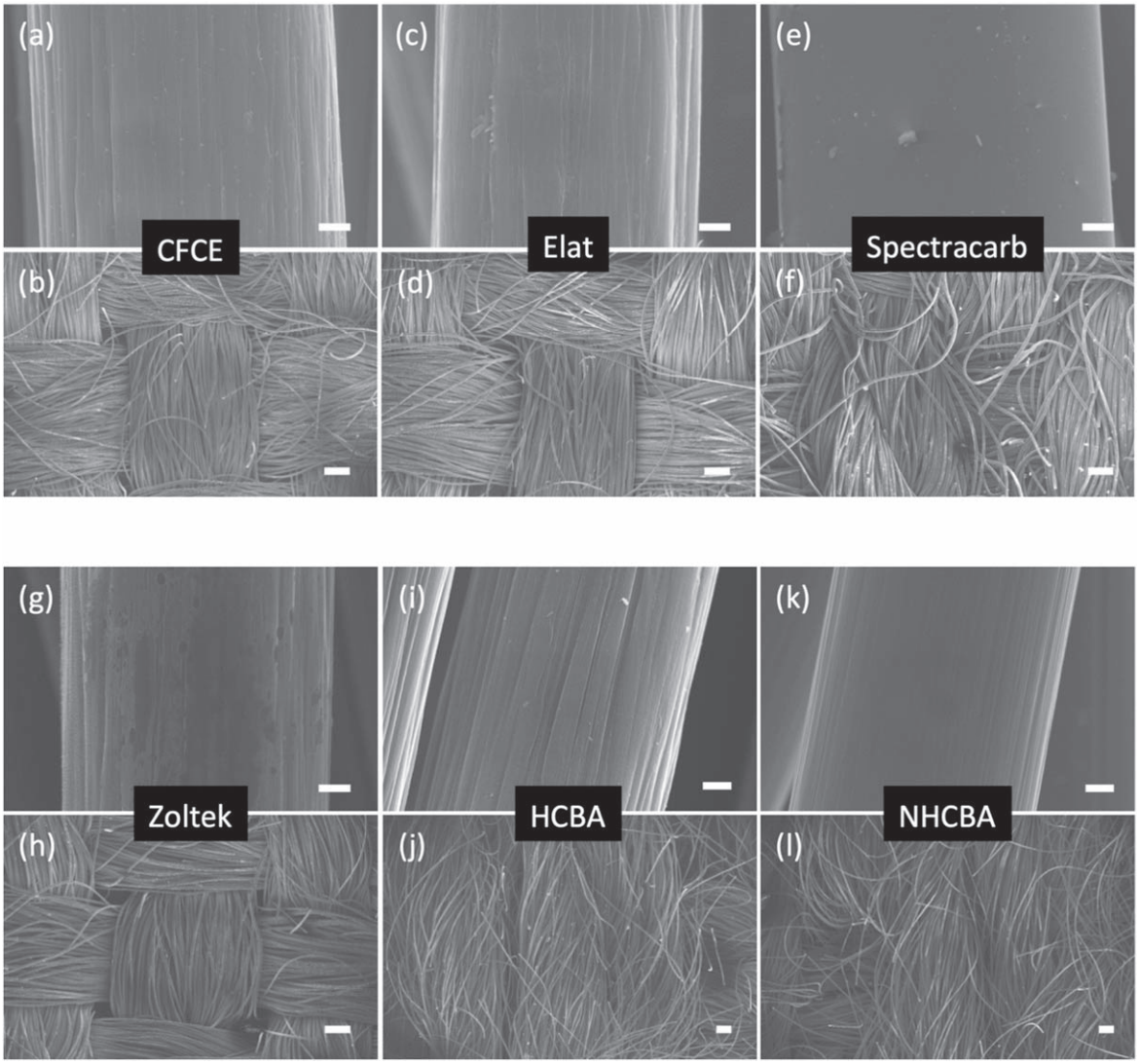

Figure 4. SEM micrographs of six carbon cloth electrodes. (a), (c), (e), (g), (i), and (k) depict a representative single fiber to observe the surface morphology (scale bar 1 μm). All fibers show minimal surface roughness or pitting at this length scale and have similar diameters. (b), (d), (f), (h), (j), and (l) depict a representative bundle and weave to observe the mesoscopic morphology of these CCEs (scale bar 100 μm). HCBA (j) has significantly lower weave periodicities (see Table I), which exceed the maximum length scale of the SEM, and NHCBA (l) has a complex weave pattern.

$$K_{TP} = \frac{-\dot{Q}\ \mu\ t}{A\ \Delta P} \quad [1]$$

where $\dot{Q}$ is the volumetric fluid flow rate, μ is the dynamic viscosity of water, t is the compressed stack thickness defined by the PTFE gasket, A is the cross-sectional flow area, and ΔP is the inlet-outlet pressure difference. Also following the work of Feser et al., a radial permeability solution linearized in fluid pressure can be written as

$$K_{TP} = \frac{-\dot{Q}\ \mu\ \ln(r_e/r_{in})}{2\pi\ t\ \Delta P} \quad [2]$$

where r_e and r_{in} are the exit (0.5 in) and inlet (0.125 in) radii respectively of the permeability apparatus. Inlet flow rate varied between 0 and 200 ml min^{-1}, and all measured pressures below 30 psig were recorded.

The permeability values in Fig. 8 can each be approximated by a unique exponential function ($R^2 > 0.95$) detailed Table SI. These fits are used for the subsequent permeability calculations as functions of strain for each electrode.

The same apparatus was used to measure through-plane electrical resistance and resistivity as functions of strain (Fig. 9). Though the electrode resistance can be approximated in a similar fashion to the permeability, we chose instead to interpolate the measured results, allowing for discontinuous behavior that arises when the electrode is irreversibly compressed. Whereas fluid permeability in a Darcy regime is strongly a function of void fraction and therefore of compressed thickness, the electrical conductivity of woven carbon cloth electrodes has multiple contributing factors including contact resistance, percolation density, and irreversible deformation. Exploration of these parameters is beyond the scope of this work, but may become relevant for future studies, particularly as higher compressive forces are applied to the electrodes.

Following a similar procedure to that of Gerhardt et al.,[17] we combine the area specific resistance measured from electrode Ohmic ASR, defined as ASR_{ohmic}, with an effective hydraulic ASR contribution from pumping, later defined as ASR_{pump}, calculated from the measured permeability. Area specific resistance due to pumping losses through a porous material is a function of the flow field geometry employed. Adapted from Gerhardt et al. the pressure drop, ΔP, is given as

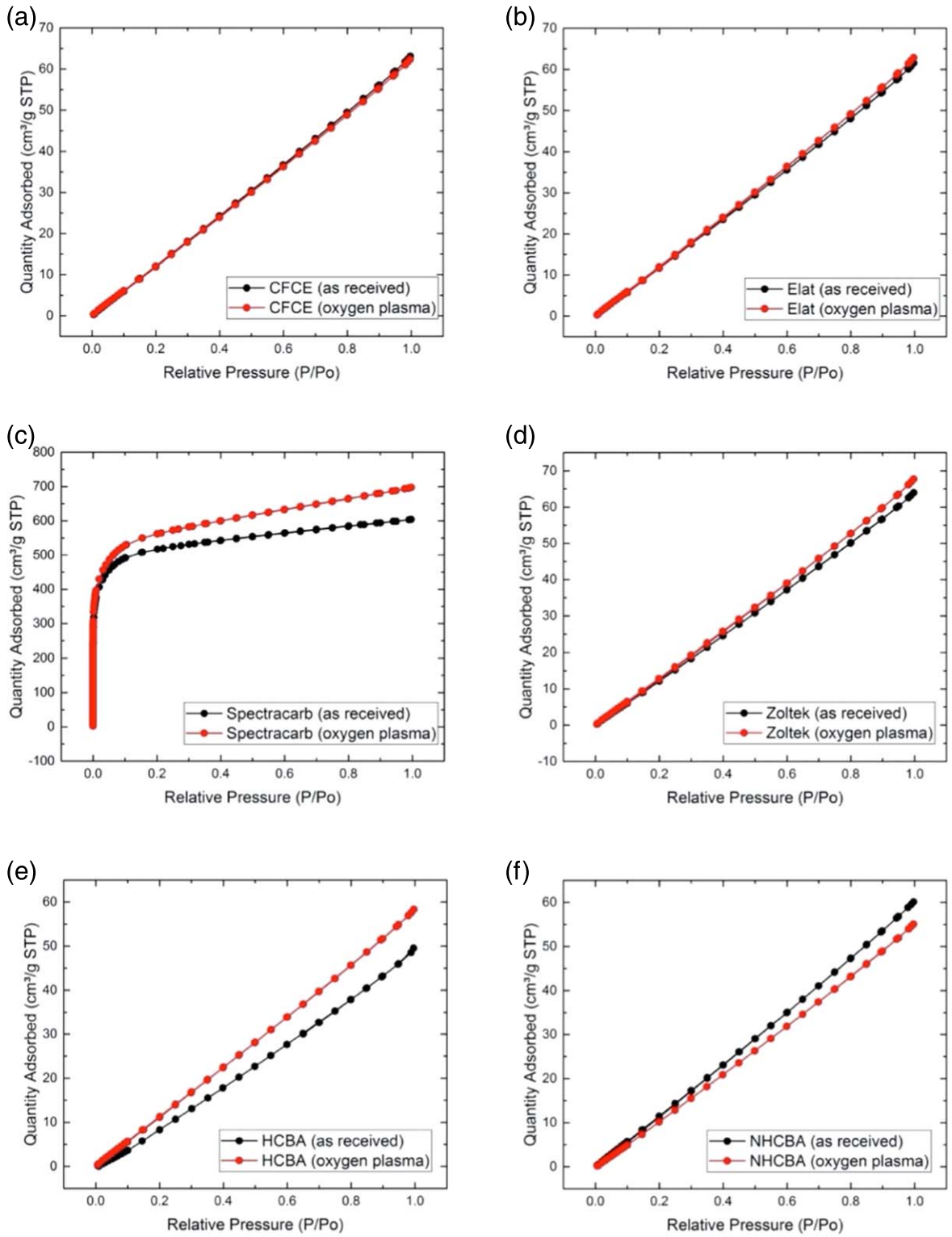

Figure 5. BET measurements of adsorbed N_2 atoms on the electrode surface as functions of partial pressure. For all experiments, the surface area of the oxygen plasma-treated electrodes (red) does not change significantly from the as-received (black) samples. Slight deviations between the pre- and post-treatment are attributed to sample-to-sample variation. The high adsorption of the Spectracarb (c) electrode at low partial pressures is indicative of high nano-scale porosity, far below the feature sizes observable in Fig. 4.

$$\Delta P = \frac{2\dot{Q}\,\mu\,(W_C + W_L)W_L}{A\,t\,K(t)} \qquad [3]$$

where W_C is the flow field channel width, W_L is the flow field landing width, and $K(t)$ is the measured permeability as a function of compressed thickness. Also from Gerhardt et al. the effective voltage efficiency loss from pumping only, ΔVE_{pump}, can be calculated as

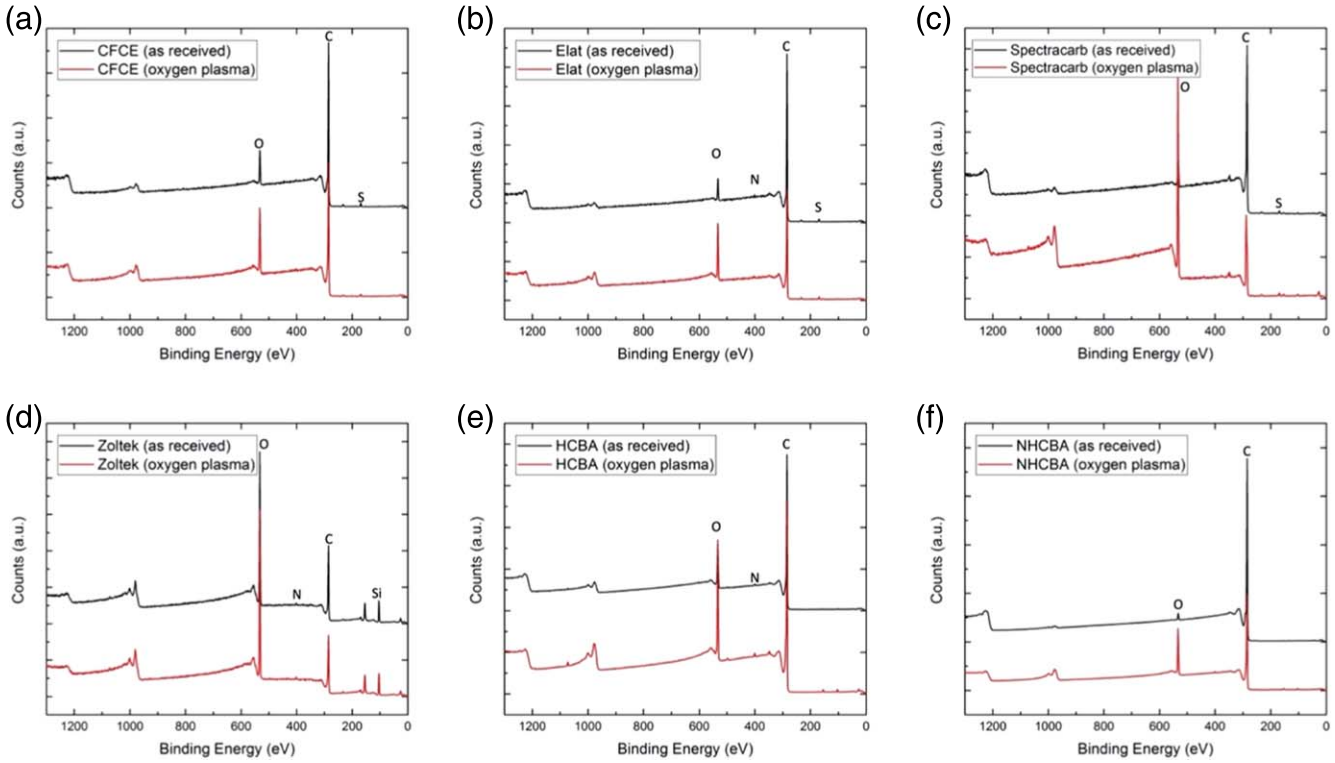

Figure 6. XPS full spectrum scans of each electrode both pre- (black) and post-(red) treatment with detectable elements labeled. All spectra show a decrease in the carbon peak (C) and increase in the oxygen peak (O) after treatment. Several trace elements are observed, most below 2 at%, in each electrode. Trace sulfur (<2 at%) is identified as the only significant impurity in the CFCE (a) and Spectracarb (c) electrodes. The Elat (b) electrode contains 1 at% nitrogen in addition to 1 at% sulfur. Zoltek (d) is the outlier containing ~13 at% silicon in addition to trace (<1 at%) nitrogen. HCBA (e) and NHCBA (F) are nearly pristine, through the former contains a measurable (<0.5 at%) nitrogen.

$$\Delta VE_{pump} = -S\frac{\dot{Q}\ \Delta P}{A\ i\ V_{OC}} \quad [4]$$

where i is the current density, V_{OC} is the full cell open circuit voltage, and S is a pump efficiency scaling factor,

$$S = \frac{1}{\psi_{pump}}\frac{\mu'}{\mu} \quad [5]$$

Here, ψ_{pump} is the fluid pump efficiency, μ is the reference viscosity, and μ' is the electrolyte viscosity, allowing for changes in viscosity.[17] Equation 4 can be rearranged and both sides divided by i to give the effective hydraulic ASR contribution from pumping, ASR_{pump},

$$ASR_{pump} \equiv -\frac{\Delta VE_{pump} V_{OC}}{i} = S\frac{\dot{Q}\ \Delta P}{A\ i^2}. \quad [6]$$

Note that we can combine Eqs. 3 and 6 and isolate the flow rate, area, and current density terms,

$$ASR_{pump} = \frac{\dot{Q}^2}{A^2\ i^2} S\frac{2\ \mu\ (W_C + W_L) W_L}{t\ K(t)}. \quad [7]$$

We define the utilization, U, as the ratio of the electronic current density to the maximum available current density given an area-specific volumetric flow rate $\dot{Q}/A$ of an electrolyte fluid,

$$U = \frac{i\ A}{\dot{Q}\ c\ F\ n}, \quad [8]$$

where F is Faraday's constant (96485 C mol^{-1}), and n is the number of transferrable electrons per molecule of reactant, and c is the concentration of the capacity-limiting reactant. For example, in a symmetric-cell configuration with a common reservoir of potassium ferri/ferrocyanide (0.1 M $K_4Fe(CN)_6$, 0.01 M $K_3Fe(CN)_6$), c would be 0.01 M from the $K_3Fe(CN)_6$ regardless of the polarization direction leading to a symmetry about the origin as seen in Figs. 10 and 11. By this definition, c is state of charge (SOC) dependent, and can change depending on the charge-discharge direction. The compressed thickness is converted to a function of engineering strain, ε, by the relationship

$$t = t_0(1 - \varepsilon) \quad [9]$$

where t_0 is the uncompressed electrode thickness. Equations 7–9 can be combined to give an effective hydraulic pumping area specific resistance from pumping as a function of electrolyte utilization and engineering strain.

$$ASR_{pump} = \frac{(c\ F\ n)^2}{U^2} S\frac{2\ \mu (W_C + W_L) W_L}{t_0(1 - \varepsilon) K(\varepsilon)}. \quad [10]$$

Gerhardt et al. show that there exists a broad optimal flow field geometry for a similar redox flow battery configuration;[17] therefore, we used the dimensions for the "Equal" flow field configuration in that reference with $W_C = W_L = 0.8$ mm to work within that optimum range. It should be noted that this geometry might not necessarily be ideal for these specific CCEs, particularly given the variation in morphology. Co-optimization of flow fields and electrodes is beyond the scope of this paper but may be an interesting avenue of research in the future.

Figure S3 depicts the combined pumping losses, ASR_{pump}, and ohmic resistive losses, ASR_{ohmic}, for a range of strains and electrolyte utilizations. These figures assume a 0.1 M concentration of

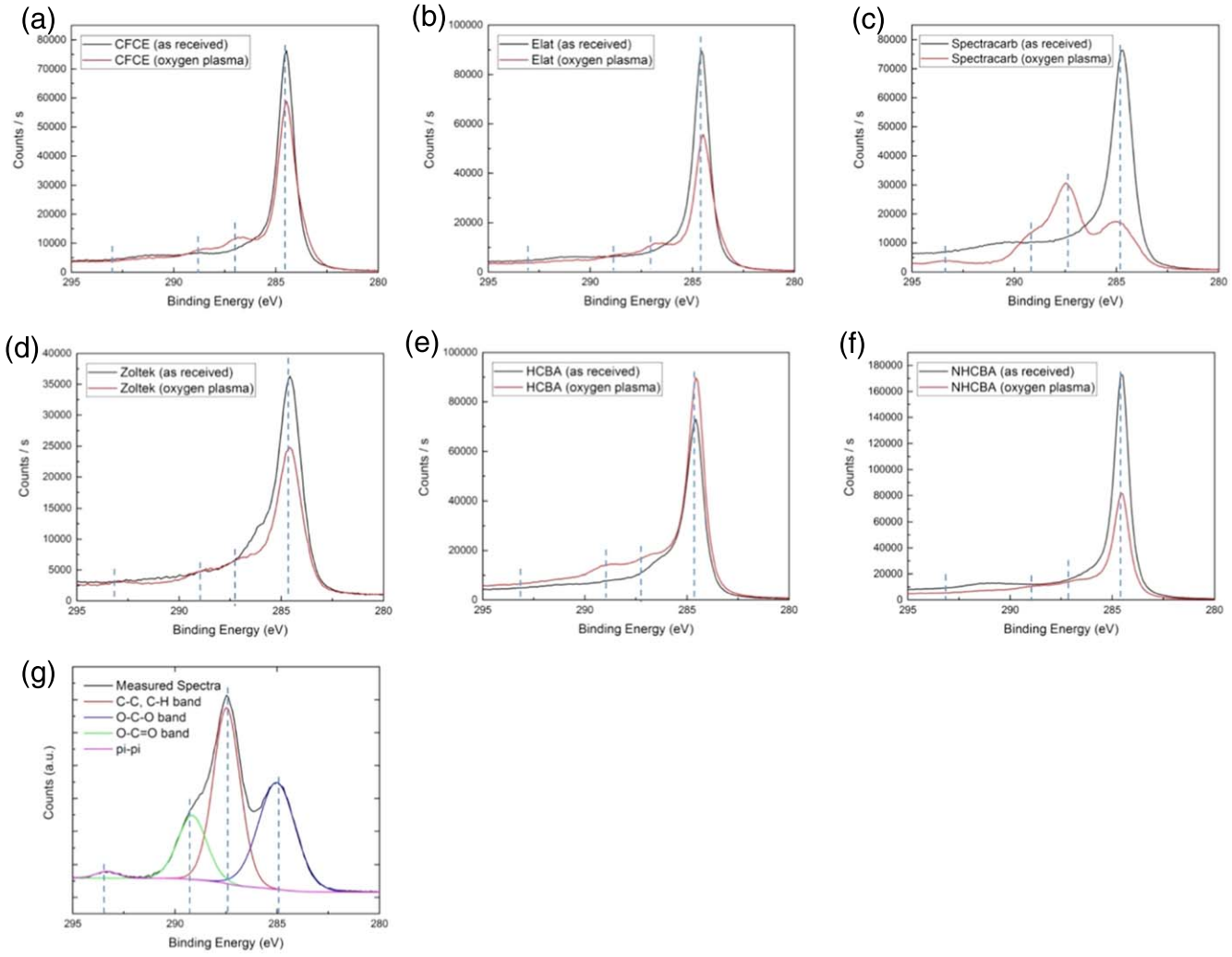

Figure 7. XPS high-resolution of the carbon peak. (g) Deconvolution of the Spectracarb post-treatment spectrum in panel (c), identifying the location of the C–C/C–H, C–O=O, C–O–C, and π-π peaks. The dotted blue lines in each sub figure mark the locations of these peaks. All post-treatment scans exhibit a relative increase in carbon-oxygen bonds.

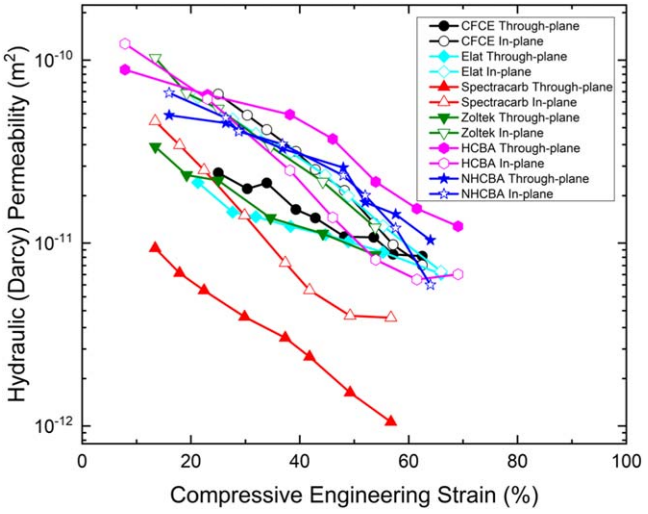

Figure 8. Hydraulic (Darcy) permeability as a function of strain. All electrodes have very similar permeabilities, except for Spectracarb (red), which has a significantly lower in-plane and through-plane permeability, particularly at high strains.

$K_4Fe(CN)_6$ ($n = 1$), 1 mPa·s viscosity, and $S = 1.67$ (~60% pump efficiency). These values are strongly dependent on active electrolyte concentration as will be explored later. The red dots mark the minimum ASR at every increment of utilization. It is evident at this stage that the Spectracarb performs significantly worse than the other electrodes. Interestingly, at intermediate (3%–5%) utilizations all electrodes show the lowest effective ASR ($ASR_{pump} + ASR_{ohmic}$) around 50% strain.

Because of this last observation, we assemble symmetric cells with 40%–60% strain on the CCEs to measure the mass transport overvoltage of the cell as the electrolyte is consumed. Flow through flow fields (Figs. S1a and S1c) in this experiment allowed for complete consumption of electrolytes at reasonably low potentials. Experiments with CFCE, Elat, and Zoltek use two layers of electrodes per side to minimize the pressure drop across the cell and prevent it from leaking at high flow rates; because of the high electrical resistance of the Spectracarb electrode, only one layer was used, and even that exhibited poor performance. Figure 10 shows the symmetric cell polarization, measured by fixing the voltage and averaging a chronoamperometry (CA) scan with a common $K_3Fe(CN)_6/K_4Fe(CN)_6$ electrolyte with 0.01 M and 0.1 M concentrations respectively. Ferricyanide ($K_3Fe(CN)_6$) is always the limiting reactant regardless of the polarization direction. Large error bars are attributed to measurement variations from the peristaltic pump pulsations. At low flow rates, the onset of a mass transport limited current is evident, with Ohmic resistive losses dominating

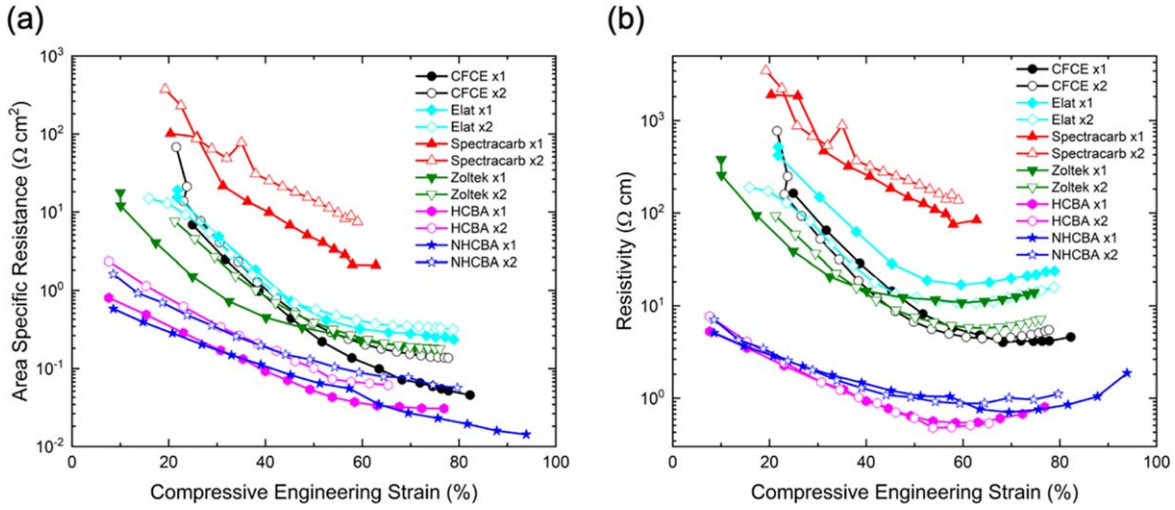

Figure 9. (a) Semi-log plot of area specific resistance (ASR) of dry electrode vs strain. All experiments were conducted with sequentially increasing strain. Electrode ASR is a strong function of strain and can change by several orders of magnitude under mild compression. Spectracarb (red) exhibits characteristically high ASR whereas HCBA and NHCBA have low ASRs across a wide range of strains. The data from (a) is converted from ASR to resistivity in (b), incorporating the compressed electrode thickness to yield an intrinsic property measurement. Note that some of the strains achieved here are impractical for an assembled cell.

with higher volumetric flow rates due to the lower electrolyte utilization. We attribute the slight asymmetry of the data to slight differences in flow rates between the two sides.

Electrochemical impedance spectroscopy (EIS) (Fig. S4) was used to deconvolute the Ohmic and charge transfer resistances within the cell. The theory behind the deconvolution is both sophisticated and debated in the electrochemical community. However, here a simplified equivalent circuit (Fig. S5c) of a Randles cell model is used, where R_S is the high frequency (electronic, ionic, and membrane) resistance, R_{CT} is the charge transfer resistance, W_P is the semi-porous (open boundary finite-length) Warburg impedance, and C is the double layer capacitance.[23] The double layer capacitance for each electrode is reported in Table SII. Figs. S5a and S5b give examples of the fit for the equivalent circuit in (c) to representative EIS spectra. Figures S4a–S4f have had the R_S subtracted to adequately compare the R_{CT}, qualitatively seen by width of the first semicircle. Though mass transport contributions are not calculated from EIS, the effect can be seen by the size of the second semicircle. At increasing flow rates, mass transport polarization decreases due to adequate supply of electrolyte to the electrode surface, resulting in a smaller second semicircle. At low flow rates, the polarization resistance increases, due to reactive species depletion on the electrode surface, characterized by a larger semicircle. Robust explanation of interpreting EIS can be found in other work.[23]

To evaluate mass transport losses, the Ohmic and kinetic overpotentials, reckoned from the ASRs from EIS (Table SII), are subtracted from the symmetric cell polarization. In systems such as ours with rapid redox kinetics, the charge transfer overpotential is essentially Ohmic and can be characterized by a charge transfer ASR that is essentially independent of current density.[24] The current density is also normalized by the volumetric flow rate. Thus, we obtain the mass transport overpotential as a function of electrolyte utilization, shown in Fig. 11. The asymmetry and scatter in some of the figures is due to slight differences in the volumetric flow rate on each side of the cell, non-adjustable because the same peristaltic pump head controls both inlets. Surprisingly, all of the electrodes with the exception of the Spectracarb have very similar mass transport overpotential trend with the limiting utilization approaching 70%–90%.

The thermodynamic overpotential of an electrochemical cell due to a variation in concentration of an oxidized and reduced species is given by the Nernst equation,

$$E = E^{0'} + \frac{RT}{nF} \ln\left(\frac{[O]}{[R]}\right), \qquad [11]$$

where $E^{0'}$ is the formal potential of the redox couple, R is the universal gas constant, and [R] and [O] are the concentrations of the reduced and oxidized species respectively. In the ferricyanide-limited half reaction, the concentration of the oxidized species decreases and the concentration of the reduced species increases by Δc, determined by the faradaic current. This leads to an effective surface potential of

$$E = E^{0'} + \frac{RT}{nF} \ln\left(\frac{[R]\Delta c}{[O] - \Delta c}\right). \qquad [12]$$

We hypothesize that the mass transport overpotential takes on a similar form as a function of the utilization, based on the expectation of proportionality between the utilization and Δc. We therefore assume the following functional form for the mass transport overpotential:

$$\eta_{MT} = \beta \frac{RT}{nF} \ln\left(\frac{1 + U/U^*}{1 - U/U^*}\right), \qquad [13]$$

where U^* is the mass transport limited utilization, defined from Eq. 8 with i replaced by the limiting current density i^*. The fitting parameter β scales the curves in Fig. 11 vertically. The black lines in Fig. 11 trace Eq. 13 with the fitting parameters for each graph. The values are given in each legend and in all cases, $\beta \approx 1.5$ Other reports have developed a more formal treatment of the mass transport overpotential incorporating both a Nernst and a Butler-Volmer overpotential contribution;[25] however, we find the simple treatment presented here to adequately account for our results.

Though the mass transport overpotential is low at small utilizations, this term can be significant for a low concentration electrolyte, or while operating near extreme SOCs. Therefore, Fig. S3 can be modified for a specific operating condition, including electrolyte utilization-induced mass transport losses. To align with the full-cell polarization experiments, we use a volumetric flow rate of 100 ml min^{-1} and an electrode area of 5 cm^2 (20 ml min^{-1} cm^{-2}), enabling a conversion from utilization to applied current density. The ASR is then multiplied by the current density to give an overvoltage; here

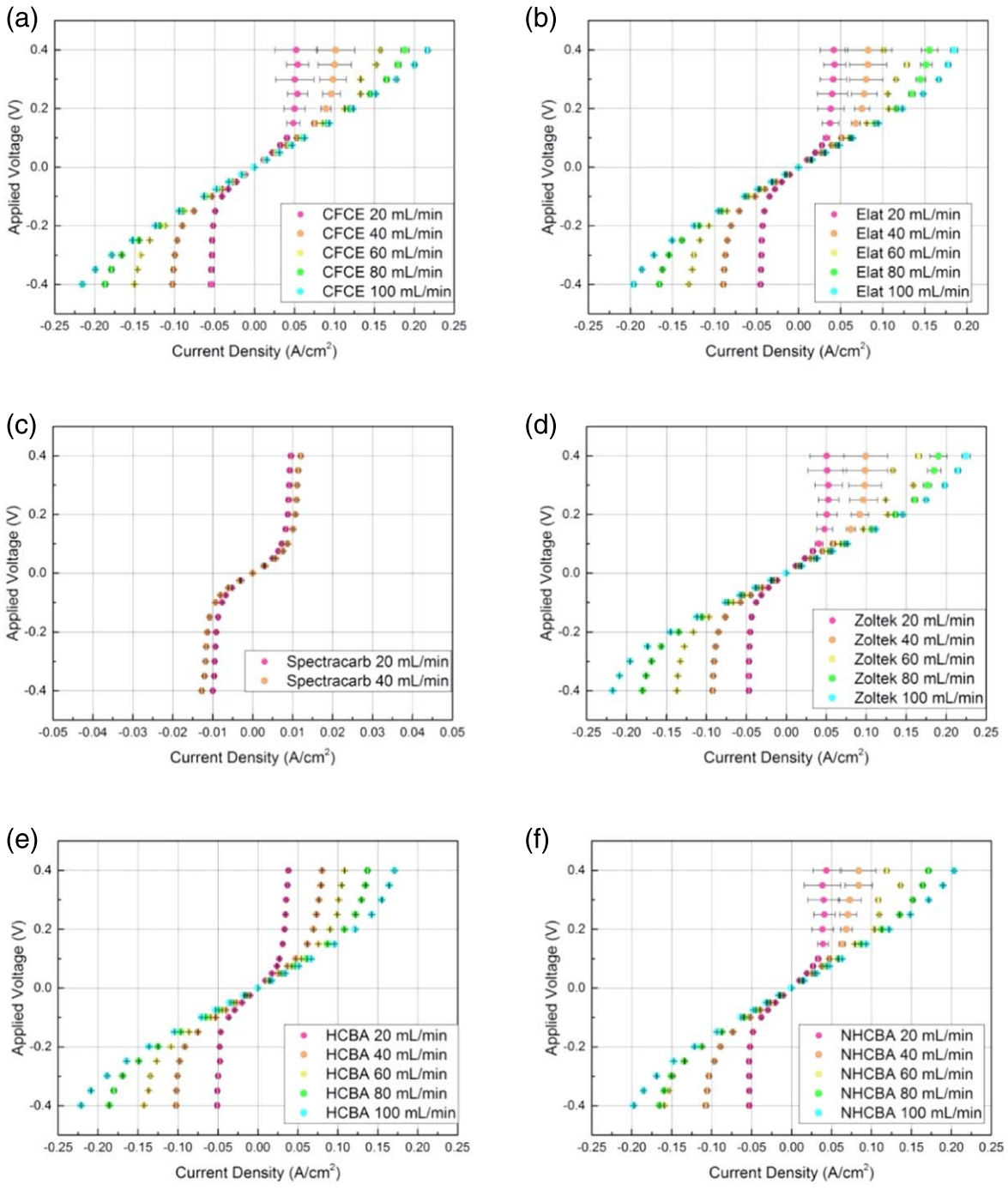

Figure 10. Symmetric cell polarization using a 5 cm^2 flow-through flow field with a common reservoir of 0.1 M $K_4Fe(CN)_6$, 0.01 M $K_3Fe(CN)_6$ at varying volumetric flow rates, measured by steady state chronoamperometry (CA). The low permeability of the Spectracarb (c) electrode caused a higher pressure drop and corresponding leakage for experiments at higher flow rates. Error bars give the standard deviation of the CA data, caused by pulsations in the peristaltic pump.

we assume a full cell potential of 1.05 V, based on reports for the DBEAQ-$K_4Fe(CN)_6$ cell.[18] A single-electron electrolyte concentration of 0.5 M and a 60% pump efficiency are used.

The results of this calculation are shown in Fig. 12, with the red dots marking the point of lowest overvoltage (highest operating cell voltage) for a given current density. Here, overvoltage is a function of current density, giving a global maximum operating voltage with corresponding strain and current density as can be seen in Fig. S6. It should be noted this result combines the electrode Ohmic, hydraulic, and mass transport overvoltages, but does not include membrane resistance which is known to be a significant contributor to Ohmic resistance. The effects of membrane resistance are discussed in the Supplementary Information because evaluations of membrane properties in electrochemical cells have been reported extensively in other work.

These results also highlight the electronic Ohmic loss as a significant limitation of these particular CCEs. Without a considerably greater compressive force, the 70%–80% compression at high current densities suggested by this analysis is not attainable within these electrodes. Furthermore, at very high compressive forces, the mechanical integrity of the membrane needs to be carefully considered to prevent membrane punctures. Therefore, we suggest

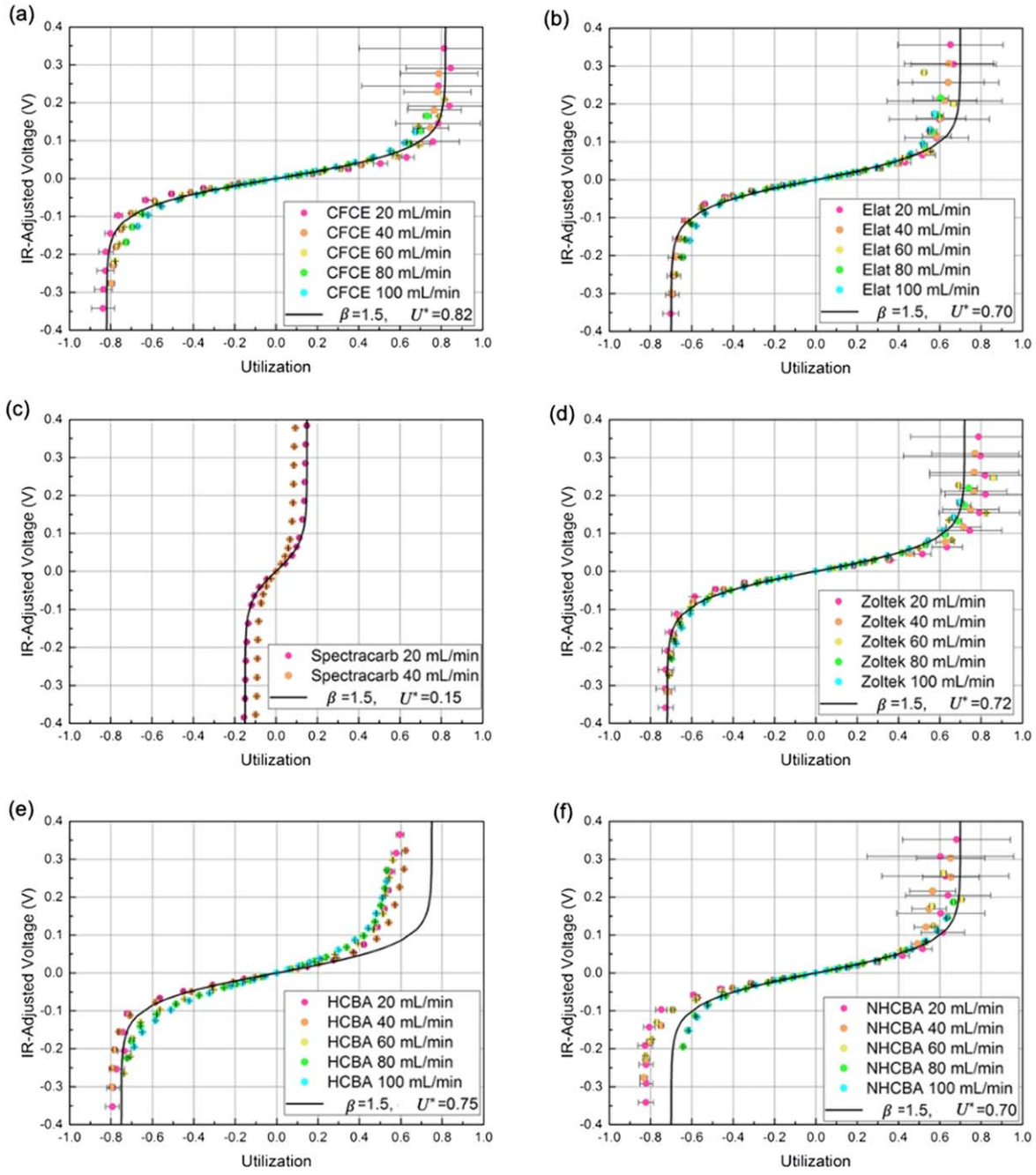

Figure 11. IR-corrected overvoltage as a function of utilization. These figures take the data from the symmetric cell polarization experiments in Fig. 10 and subtract the high-frequency and charge transfer resistances recorded in Table SII. Current density is then normalized according to Eq. 8 to obtain a utilization. Asymmetries between the positive and negative utilizations are attributed to differences in pumping velocities between the two sides of the cell. The black line represents a fit for data using Eq. 13. Values for the fitting parameters β and U^* are reported in the figure legends.

that future CCE engineering should focus on reducing Ohmic resistance at lower strains, enabling improved performance without compromising the mechanical integrity of the cell components. As stated previously, several overlapping factors including contact resistance, percolation density, and irreversible deformation contribute to the electrode Ohmic resistance, so further research will be needed to validate this suggestion.

Because only the posolyte was tested for the mass transport and kinetic overpotential contributions at different utilizations, we make several assumptions for the negolyte. First, we assume that for an organic quinone, n = 2, effectively doubling the electrolyte capacity. Second, we assume the mass transport and reaction kinetics are approximately the same. Prior studies have demonstrated excellent kinetics on carbon surfaces for both the $K_4Fe(CN)_6$ and DBEAQ electrolytes.[18] On the other hand, variations in the diffusion rates of the electrolytes may impact the mass transport overpotential. Because this dominates at high utilization, we assume this has a negligible effect on the full cell performance at low electrolyte utilizations.

Often, RFBs are benchmarked by their performance at 100 mA cm^{-2}, which happens to coincide with the optimum efficiency for both the posolyte and negolytes given the assumptions stated above. For these CCEs, this optimum occurred between 50% to 60% electrode compression. Using the results from Fig. 12 and the assumptions stated above, full cells were assembled with CFCE, Elat, and Zoltek electrodes to compare their performance. Only three

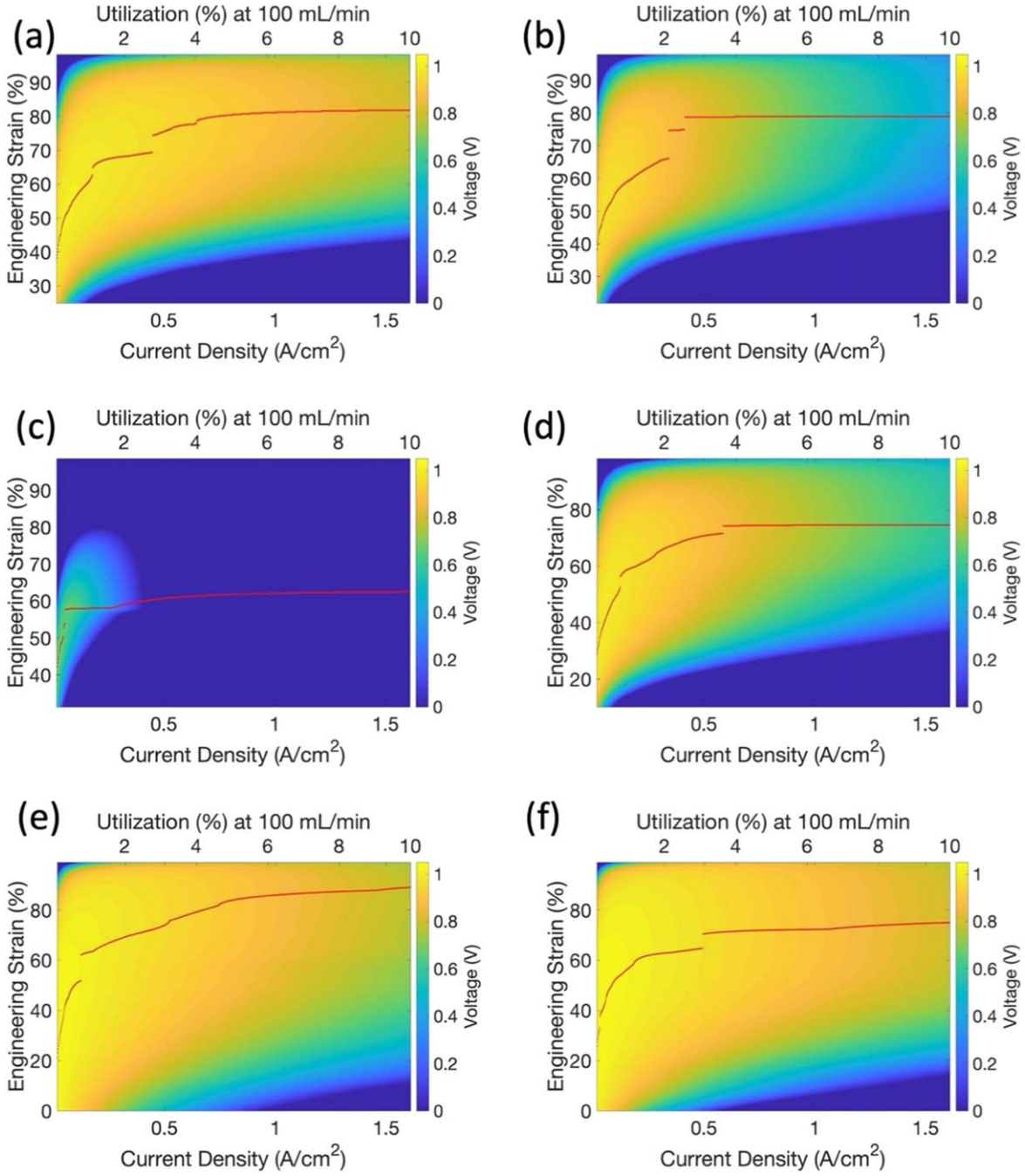

Figure 12. Calculated combined Ohmic, mass transfer, charge transfer, and pumping overvoltages as a function of strain and applied current density for (a) CFCE, (b) Elat, (c) Spectracarb, (d) Zoltek, (e) HCBA, and (f) NHCBA electrodes. Assumed here is a one-electron electrolyte at 0.5 M concentration, pumped at 100 ml min^{-1} in an IDFF described in Fig. S1. Pumping efficiency is assumed to be 60%, full cell voltage is 1.05 V, and no membrane resistance is included. Figures show up to 10% utilization to show a range of typical operating conditions. Full maps of 100% utilization are discussed in the Supplementary Information. The ideal compression calculated under these conditions is traced by the red dots in each figure, though for all but Spectracarb a fairly broad maximum occurs as a function of compression.

electrodes were evaluated in a full-cell configuration to highlight the merits of this methodology. Figure 13 shows the full cell polarization and power density curves for these three electrodes. The record peak power density for this chemistry of 0.4 W cm^{-2} at 100% SOC, a 65% increase from published results[18] is achieved in large part due to a low full cell ASR, enabled by identifying an optimum engineering and operating regime. We note that the posolyte concentration is higher and its volume smaller than in the previously published work, which can contribute to both a higher cell voltage at high SOCs, and a lower mass transport resistance. The comparison between the electrolytes and a breakdown of the improvements contributed from the cell voltage and ASR are detailed in Table SIII. These results indicate that over 60% of the peak power density increase are attributable to the decrease in full cell ASR, stemming from the improved use of the electrodes.

The high linearity of the 50%–100% SOC i-V curves in Figs. 13a, 13c, and 13e indicate mass transport effects have a minimal impact on cell performance under these operating conditions. Figure 14 highlights these effects, showing zoomed in i-V polarization (a) and power-current density (b) plots for the CFCE electrode. The full cell DC-ASR is 0.86 Ωcm^2 allowing for greater than 90% one-way voltage efficiency—approximated by the black

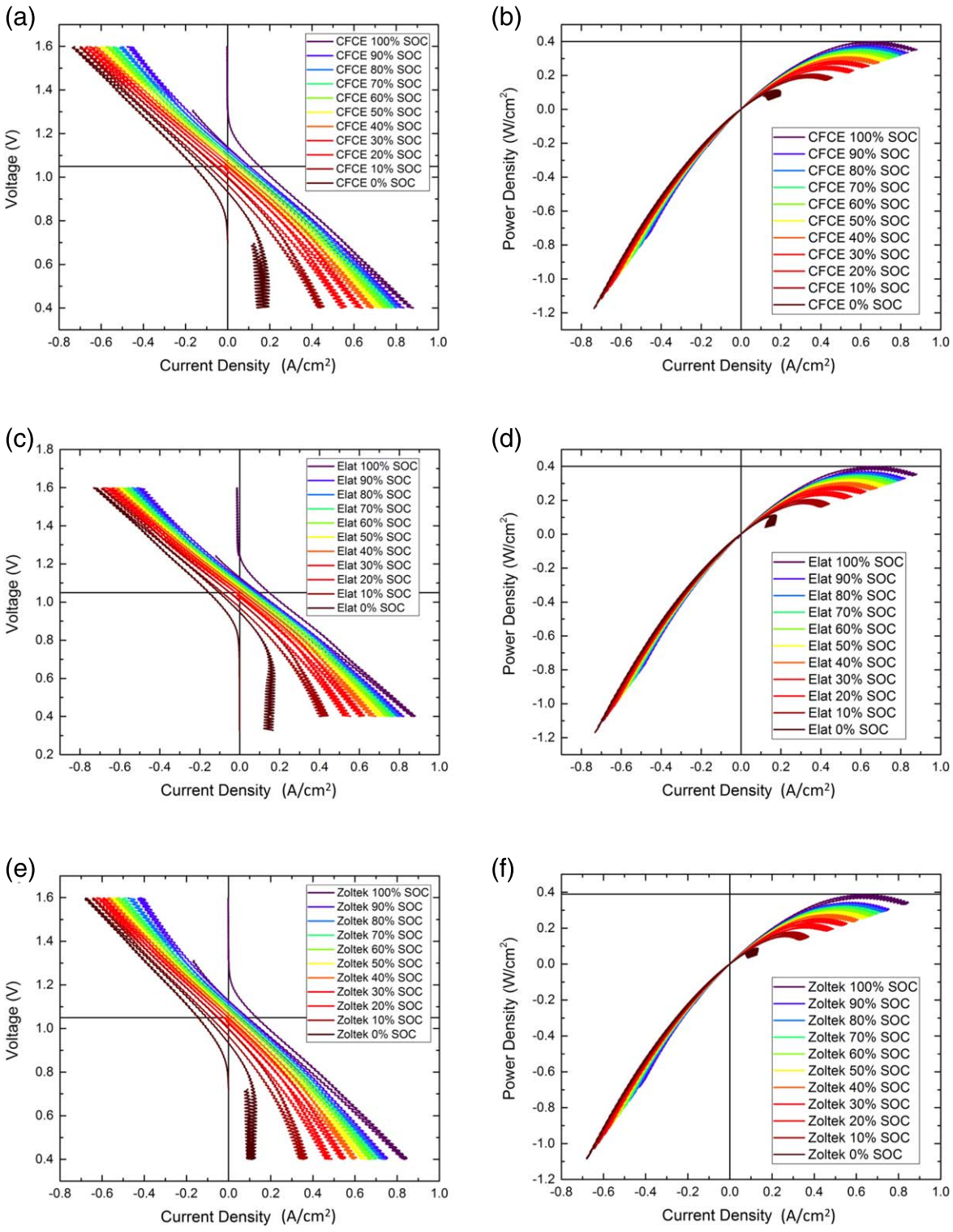

Figure 13. Full cell power density and voltage polarization curves respectively for the CFCE (a) and (b), the Elat (c) and (d), and the Zoltek (e) and (f) electrodes. Each electrode is compressed between 50 and 60% strain, and the electrolyte is 6 ml 0.5 M DBEAQ vs. 15 ml 0.5 M $K_4Fe(CN)_6$ + 0.05 M $K_3Fe(CN)_6$, all in 0.01 M KOH electrolyte. Flow rate is 100 ml min^{-1}. The peak power densities of 0.40, 0.40 and 0.39 W cm^{-2} at 100% SOC represent a 65% incrase from published data.

arrows in Fig. 14a at 50% SOC—achievable above 100 mA cm^{-2} and greater than 100 mW cm^{-2}. Figure 14c converts the power density vs current density in (b) into power density vs utilization based on the available electrolyte composition at each SOC.

Conclusions

The method presented here provides a framework for a robust comparison of the physical properties and electrochemical performance of flow-cell porous carbon cloth electrodes (CCEs), applied here to redox flow batteries (RFBs). We develop a tool for measuring in-plane and through-plane electrolyte permeability, and

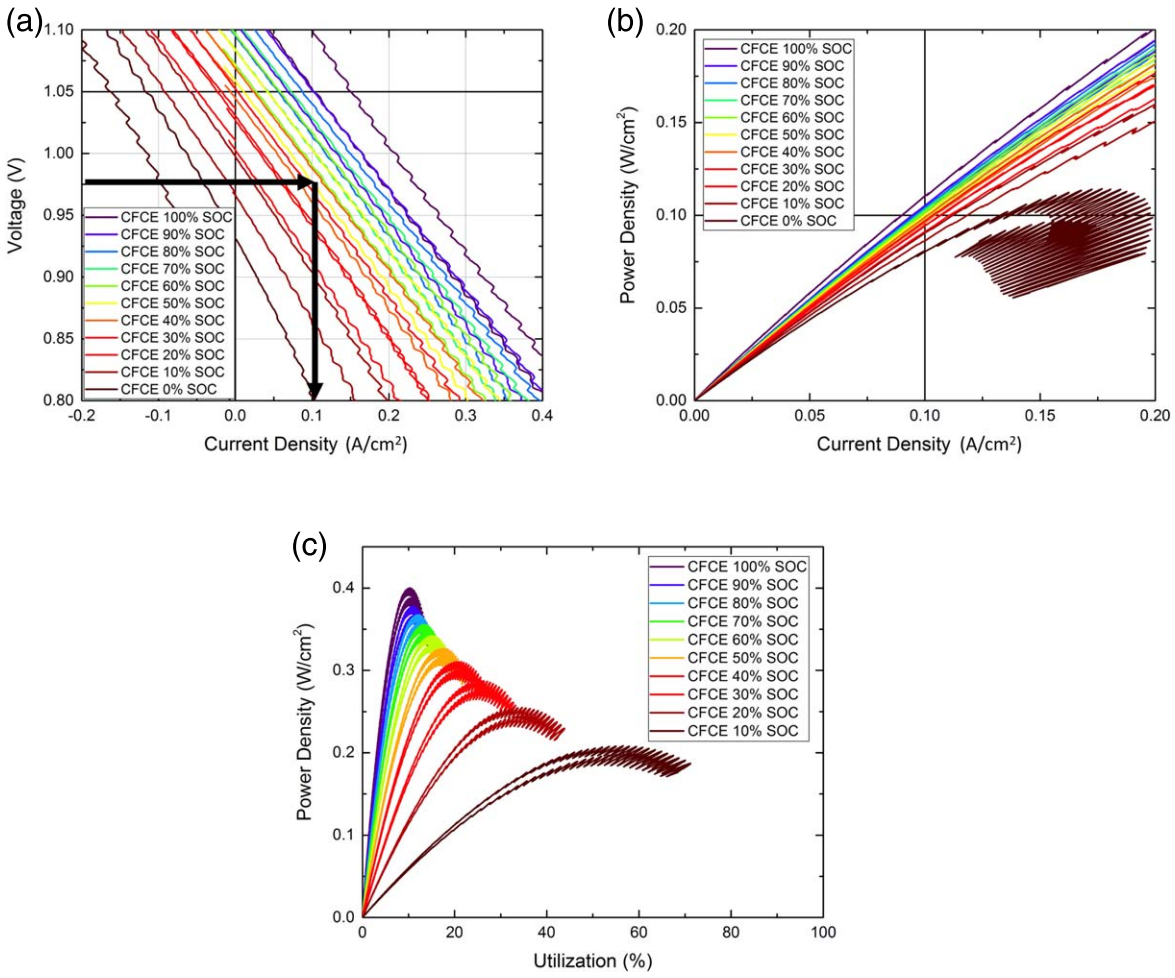

Figure 14. Results from CFCE full cell polarization experiments. (a) Zoomed in view of i-V polarization curve depicted in Fig. 13a. Slope of the curves indicates a DC-ASR of 0.86 Ωcm^2 at 50% SOC. 93% one-way voltage efficiency at 50% SOC (0.975 V) is attainable at 100 mA cm^{-2}. (b) Zoomed in view of the power density-current density curve in Fig. 13b. (c) comprises the power density curves from (b) adjusted to utilization assuming a discharge concentration of 0.5 M x SOC.

through-plane electrical conductivity, and show how these data can be incorporated into a model for electrode resistive losses. To compare electrodes, we measure Ohmic and effective hydraulic losses with this ex situ tool, and then measure the charge transfer and mass transport losses in a symmetric cell. In the symmetric cell, by subtracting the Ohmic and charge transfer losses, both obtained from electrochemical impedance spectroscopy, we isolate a mass transport loss that can be modeled by a Nernst-like empirical equation as a function of utilization (percent electrolyte conversion per pass) across a wide range of volumetric fluid flow rates. Though the ferri/ferrocyanide and quinone electrolytes used in this study exhibit fast kinetics relative to other common RFB active species, the capability of separating and directly comparing mass transport, Ohmic, and charge transfer overpotentials for kinetically facile species highlights the strength of this method. Through this analysis, we find that of the loss components in a RFB electrode—Ohmic resistance, charge transfer, mass transport, and pumping—the principal contributor is the Ohmic resistance for the flow field and electrode thicknesses examined here. Pumping losses factor in only under extreme electrode strains and as a parasitic loss at low utilizations. In contrast, mass transport losses factor in primarily at extreme states of charge or high utilizations.

Because of the low pumping losses, the results of this model indicate that compressing these particular CCEs with up to between 50%–60% strain can minimize total losses, which are largely dominated by electrode electronic resistance, when operating between 3%–5% electrolyte utilization. The model suggests higher efficiencies can be achieved at higher utilizations by increased CCE compressive strains (lower Ohmic losses), but the potential for compromising the mechanical integrity of the cell and the membrane should be weighed carefully. Future work on engineering CCEs should aim to increase the electrical conductivity at lower compressions, such that the Ohmic losses are minimized for practical strains.

Electrochemical tests using a symmetric cell configuration help deconvolute charge transfer and mass transport resistances; the former is a small but non-negligible factor in overall polarization losses, whereas the latter is of principal concern at low concentrations (extreme SOCs) and high utilization. These symmetric cell measurements, fit to the Nernst-like empirical model, enable the identification of a mass transport limited utilization to complete the model. The combined Ohmic, charge transfer, mass transport, and pumping losses are converted to overpotentials and the insights from these findings lead to the construction of a full cell RFB with low ASR (0.86 Ωcm^2) and record high peak power density (0.4 W cm^{-2}) for this RFB chemistry. This work demonstrates that carbon cloth electrodes are promising materials to use in aqueous organic redox flow batteries, and further research should be conducted to more fully assess their optimal design parameters.

Acknowledgments

This research was supported by U.S. DOE award DE-AC05-76RL01830 through PNNL subcontract 428977, by the Massachusetts Clean Energy Center, and by a gift of Allicia Lam

and Richard Powell. Manuscript preparation was performed by Andrew Wong under the auspices of the U.S. Department of Energy by Lawrence Livermore National Laboratory under Contract DE-AC52-07NA27344. The authors thank Eric Fell and Andrew Meersand for helpful discussions.

ORCID

Andrew A. Wong https://orcid.org/0000-0002-1912-7357
Michael J. Aziz https://orcid.org/0000-0001-9657-9456

References

1. A. Forner-Cuenca and F. Brushett, "Engineering Porous electrodes for next-generation redox flow batteries: recent progress and opportunities." *Current Opinion in Electrochemistry*, **18**, 113 (2019).
2. S. Lister and G. McLean, "PEM fuel cell electrodes." *J. Power Sources*, **130**, 61 (2004).
3. L. Arenas, C. Ponce de León, and F. Walsh, "Three-deimensional porous metal electrodes: fabrication, characterisation and use." *Current Opinion in Electrochemistry*, **16**, 1 (2019).
4. Z. Liu et al., "Three-dimensional ordered porous electrode materials for electrochemical energy storage." *NPG Asia Mater.*, **11**, 1-21 (2019).
5. K. Kim, M.-S. Park, Y.-J. Kim, J. Kim, S. Dou, and M. Skyllas-Kazacos, "A technology review of electrodes and reaction mechanisms in vanadium redox flow batteries." *Journal of Materials Chemistry A*, **33**, 16913-16933 (2015).
6. D. Emmel, J. D. Hofmann, T. Arlt, I. Manke, G. D. Wehinger, and D. Schröder, "Understanding the impact of compression on the active area of carbon felt electrodes for redox flow batteries." *ACS Appl. Energy Mater.*, **3**, 4384-4393 (2020).
7. A. Jayakumar, S. Singameni, M. Ramos, A. Al-Jumaily, and S. Pethaiah, "Manufacturing the gas diffusion layer for PEM fuel cell using a novel 3D printing technique and critical assessment of the challenges encountered." *Materials (Basel)*, **10**, 1-9 (2017).
8. D. Zhang, A. Forner-Cuenca, O. Taiwo, V. Yufit, F. Brushett, N. Brandon, S. Gu, and Q. Cai, "Understanding the role of the porous electrode microstructure in redox flow battery performance using an experimentally validated 3D pore-scale lattice Boltzmann model." *J. Power Sources*, **447**, 227249 (2020).
9. E. Frank, L. Steudle, D. Ingildeev, J. Sporl, and M. Buchmeiser, "Carbon fibers: precursor systems, processing, structure, and properties." *Angew. Chem. Int. Ed.*, **53**, 5262 (2014).
10. K. Tenny, A. Forner-Cuenca, Y.-M. Chiang, and F. Brushett, "Comparing physical and electrochemical properties of different weave patterns for carbon cloth electrodes in redox flow batteries." *Journal of Electrochemical Energy Conversion and Storage*, **17**, 041108 (2020).
11. A. Forner-Cuenca, E. Penn, A. Oliveira, and F. Brushett, "Exploring the role of electrode microstructure on the performance of non-aqueous redox flow batteries." *J. Electrochem. Soc.*, **166**, A2230 (2019).
12. H.-J. Ahn, J.-H. Lee, Y. Jeong, J.-H. Lee, C.-S. Chi, and H.-J. Oh, "Nanostructured carbon cloth electrode for desalination from aqueous solutions." *Mater. Sci. Eng., A*, **449–451**, 841 (2007).
13. N. Rajalakshmi, G. Velayutham, K. Ramya, C. K. Subramaniyam, and K. S. Dhathathreyan, "Characterisation and optimisation of low cost activated carbon fabric as a substrate layer for PEMFC electrodes." *Fuel Cell*, **74182**, 169-173 (2005).
14. D. Dixon, D. Babu, J. Langer, M. Bruns, L. Pfaffmann, A. Bhaskar, J. Schenider, F. Scheiba, and H. Ehrenberg, "Effect of oxygen plasma treatment on the electrochemical performance of the rayon and polyacrylonitrile based carbon felt for the vanadium redox flow battery application." *J. Power Sources*, **332**, 240 (2016).
15. K. V. Greco, A. Forner-Cuenca, A. Mulaarczyk, J. Eller, and F. R. Brushett, "Elucidating the nuanced effects of thermal pretreatment on carbon paper electrodes for vanadium redox flow batteries." *ACS Appl. Mater. Interfaces*, **10**, 44430 (2018).
16. G. C. Sedenho, D. De Porcellinis, Y. Jing, E. Kerr, L. M. Mejia-Mendoza, A. Vazquez-Mayagoitia, A. Aspuru-Guzik, R. G. Gordon, F. N. Crespilho, and M. J. Aziz, "Effect of molecular structure of quinones and carbon electrode surfaces on the interfacial electron transfer process." *ACS Appl. Energy Mater.*, **3**, 1933 (2020).
17. M. Gerhardt, A. Wong, and M. Aziz, "The effect of interdigitated channel and land dimensions on flow cell performance." *Journal of the Electrochemistry Society*, **165**, A2625 (2018).
18. D. Kwabi, K. Lin, Y. Ji, E. Kerr, M.-A. Goulet, D. De Porcellinis, D. Tabor, D. A.-G. A. Pollack, R. Gordon, and M. Aziz, "Alkaline quinone flow battery with long lifetime at pH 12." *Jouel*, **2**, 1907 (2018).
19. R. Picu, "Mechanics of random fiber networks - a review." *Soft Matter*, **7**, 6768 (2011).
20. B. Zhang, F. Kang, J.-M. Tarascon, and J.-K. Kim, "Recent advances in electrospun carbon nanofibers and their application in electrochemical energy storage." *Prog. Mater Sci.*, **76**, 319 (2016).
21. J. Ryu, M. Park, and J. Cho, "Catalytic Effects of B/N-co-Doped Porous Carbon Incorporated with Ketjenblack Nanoparticles for All-Vanadium Redox Flow Batteries." *J. Electrochem. Soc.*, **163**, A5144 (2016).
22. J. P. Feser, A. K. Prasad, and S. G. Advani, "Experimental characterization of in-plane permeability of gas diffusion layers." *J. Power Sources*, **162**, 1226 (2006).
23. S. Cooper, A. Bertei, D. Finegan, and N. Brandon, "Simulated impedance of diffusion in porous media." *Electrochim. Acta*, **251**, 681 (2017).
24. Q. Chen, M. R. Gerhardt, and M. J. Aziz, "Dissection of the voltage losses of an acidic quinone redox flow battery." *J. Electrochem. Soc.*, **164**, A1126 (2017).
25. S. Murthy, A. Sharma, C. Choo, and E. Birgersson, "Analysis of concentration overpotential in an all-vanadium redox flow battery." *J. Electrochem. Soc.*, **165**, A1746 (2018).

Method for Comparing Porous Carbon Electrode Performance in Redox Flow Batteries

Andrew A. Wong*† and Michael J. Aziz*

* Harvard John A. Paulson School of Engineering and Applied Sciences, Cambridge, Massachusetts 02138, USA
†Present Address: Lawrence Livermore National Lab, Livermore, California, 94550, USA

Supplementary Information:

Table of Contents

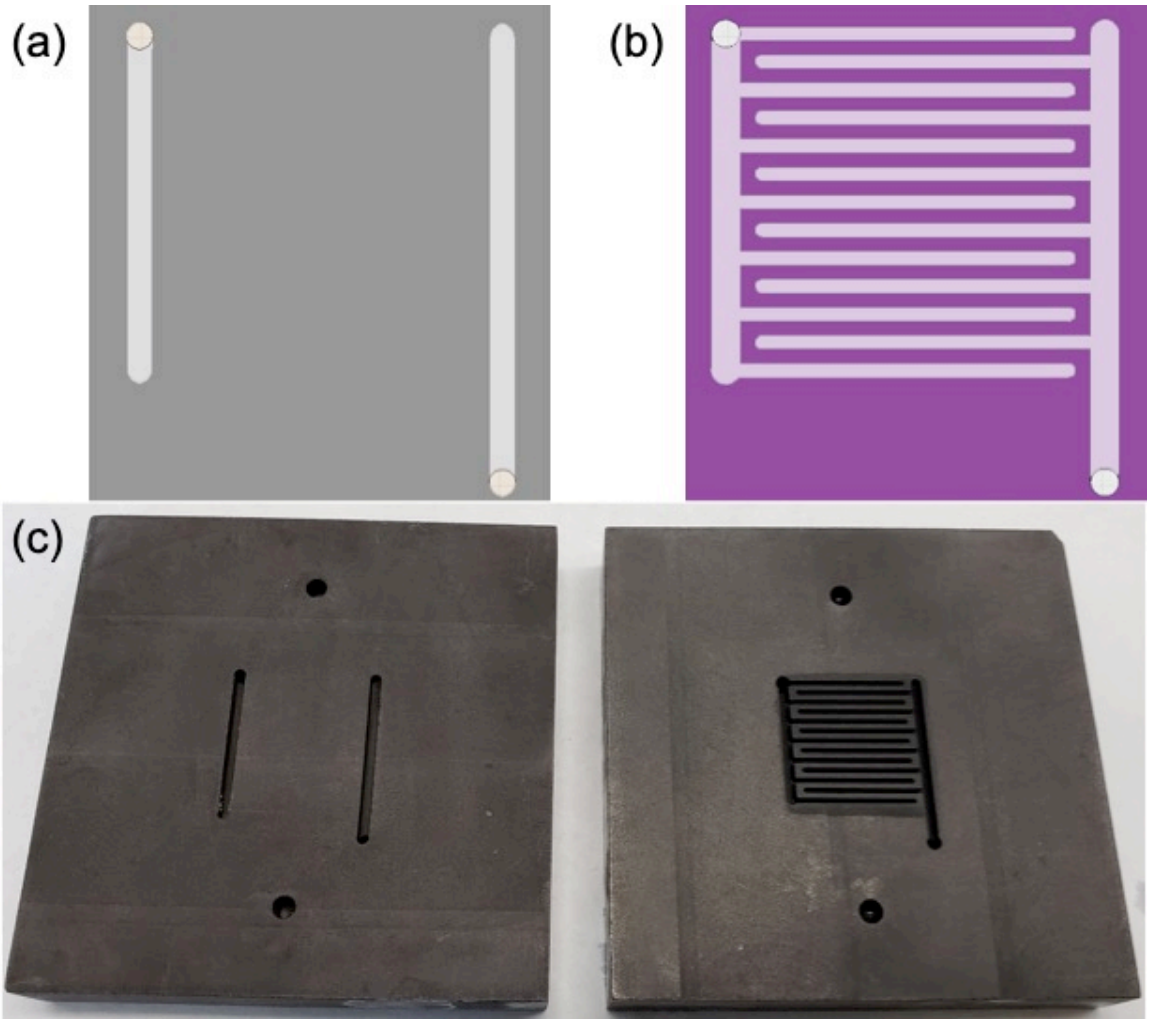

Figure S1. Drawings of (a) a flow through flow field and (b) an evenly-spaced interdigitated flow field (IDFF) with 0.8 mm channel and landing widths, with corresponding photograph (c). Flow through flow fields are used for the symmetric cell experiments, and the IDFF is used for the full cell experiments.

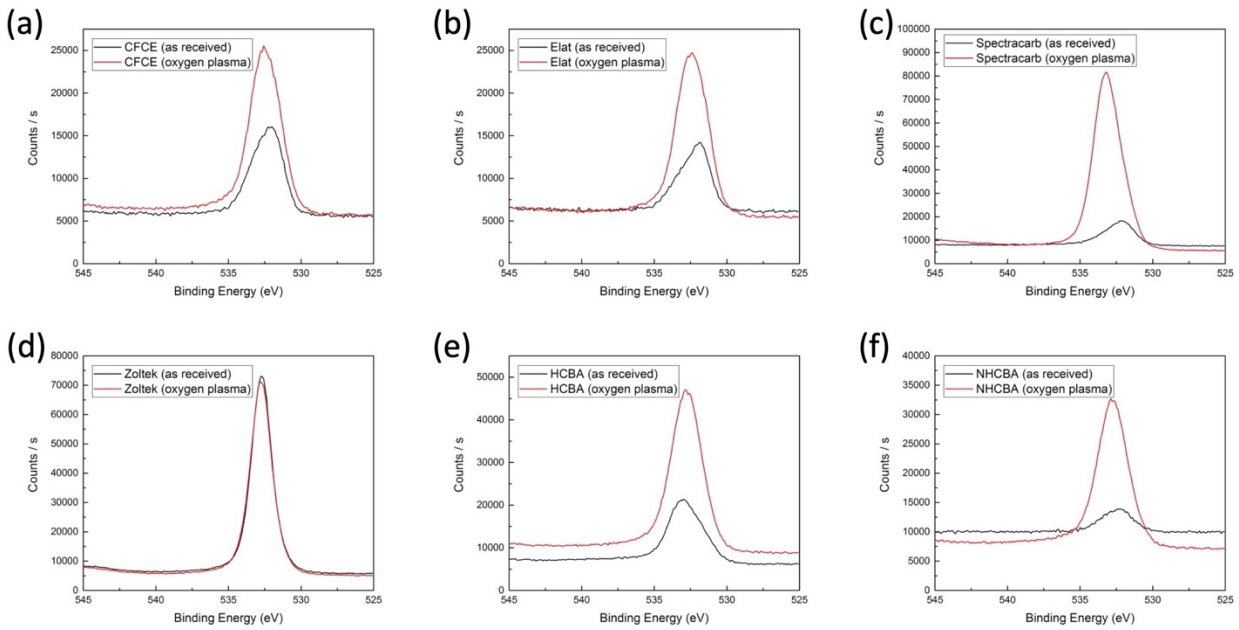

Figure S2. XPS high-resolution scans of the oxygen peak. Oxygen surface content increases substantially after oxygen plasma treatment in all samples except for Zoltek; it is evident that this electrode has a high oxygen content as received.

Figure S2 shows a high-resolution scan of the oxygen peak centered around a 532.5 eV binding energy. This result clearly indicates an increase in oxygen surface content after oxygen plasma treatment, except for the Zoltek CCE; it is possible that the high oxygen content in the as-received Zoltek sample represents a fully saturated surface functionalization, though additional tests should be conducted to confirm this.

Table S1. Equations for the exponential fits to the permeability data in Figure 8. Here ε is the engineering strain that results in the in-plane (K_{IP}) and through-plane (K_{TP}) permeabilities (m^2) for each electrode.

Electrode $\boldsymbol{\varepsilon}$ = eng. strain (%)	CFCE	Elat	Spectracarb
1-electrode K_{TP} (m^2)	$(5.1E\text{-}11)e^{-3.0\boldsymbol{\varepsilon}}$	$(3.1E\text{-}11)e^{-2.3\boldsymbol{\varepsilon}}$	$(1.7E\text{-}11)e^{-4.9\boldsymbol{\varepsilon}}$
K_{IP} (m^2)	$(3.0E\text{-}10)e^{-5.9\boldsymbol{\varepsilon}}$	$(1.9E\text{-}10)e^{-4.9\boldsymbol{\varepsilon}}$	$(9.7E\text{-}11)e^{-6.3\boldsymbol{\varepsilon}}$
	Zoltek	HCBA	NHCBA
1-electrode K_{TP} (m^2)	$(4.8E\text{-}11)e^{-3.3\boldsymbol{\varepsilon}}$	$(1.4E\text{-}10)e^{-3.4\boldsymbol{\varepsilon}}$	$(1.0E\text{-}10)e^{-3.4\boldsymbol{\varepsilon}}$
K_{IP} (m^2)	$(1.9E\text{-}10)e^{-5.1\boldsymbol{\varepsilon}}$	$(1.8E\text{-}10)e^{-5.3\boldsymbol{\varepsilon}}$	$(1.6E\text{-}10)e^{-4.6\boldsymbol{\varepsilon}}$

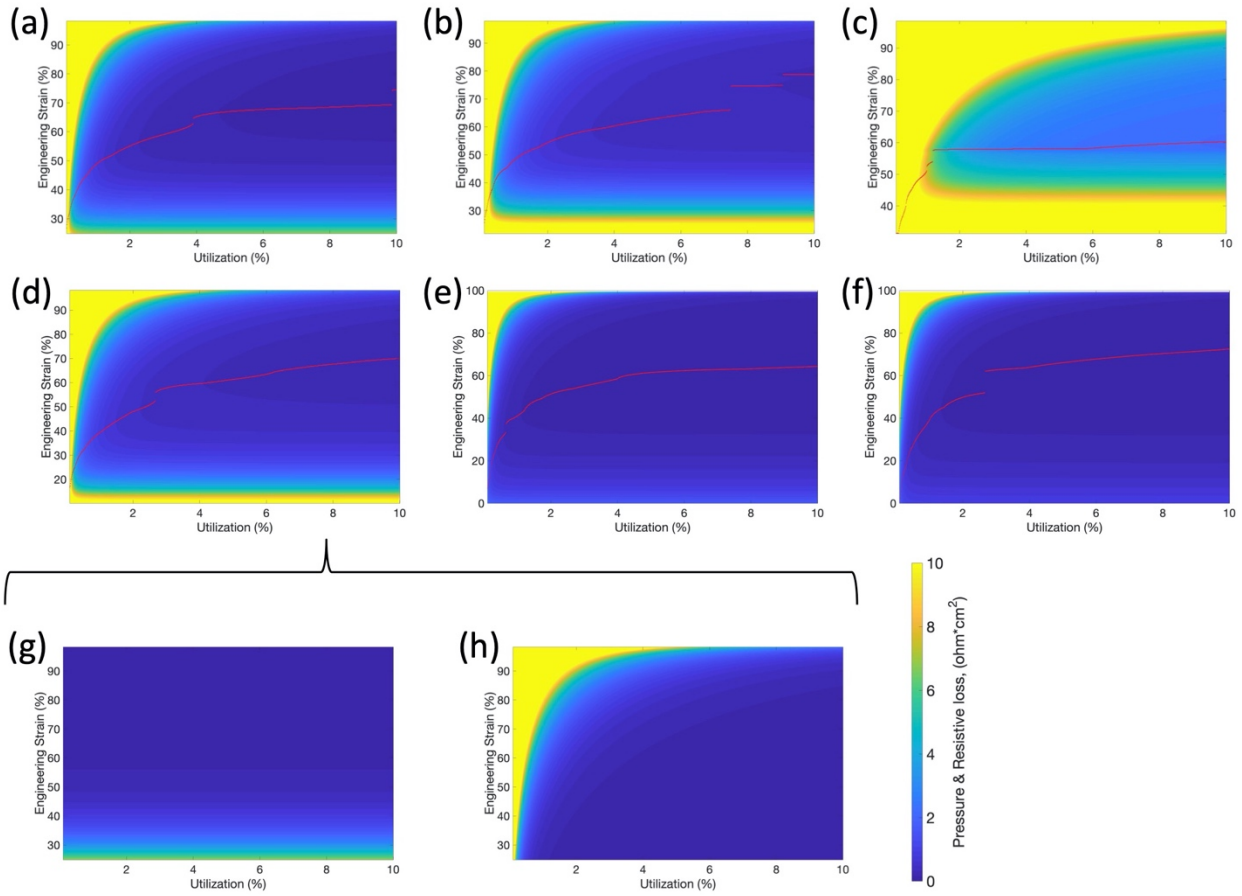

Figure S3. Combinations of Ohmic and hydraulic losses as a function of strain and electrolyte utilization for (a) CFCE, (b) Elat, (c) Spectracarb, (d) Zoltek, (e) HCBA, and (f) NHCBA electrodes. Red dots indicate the optimum strain at every value of utilization to minimize losses. Losses are indicated for a half-cell and should be double counted when considering full cell losses, but this does not impact the location of the strain for minimum losses. (g) and (h) show the Ohmic losses and hydraulic losses respectively, highlighting the operating conditions most impacted by each.

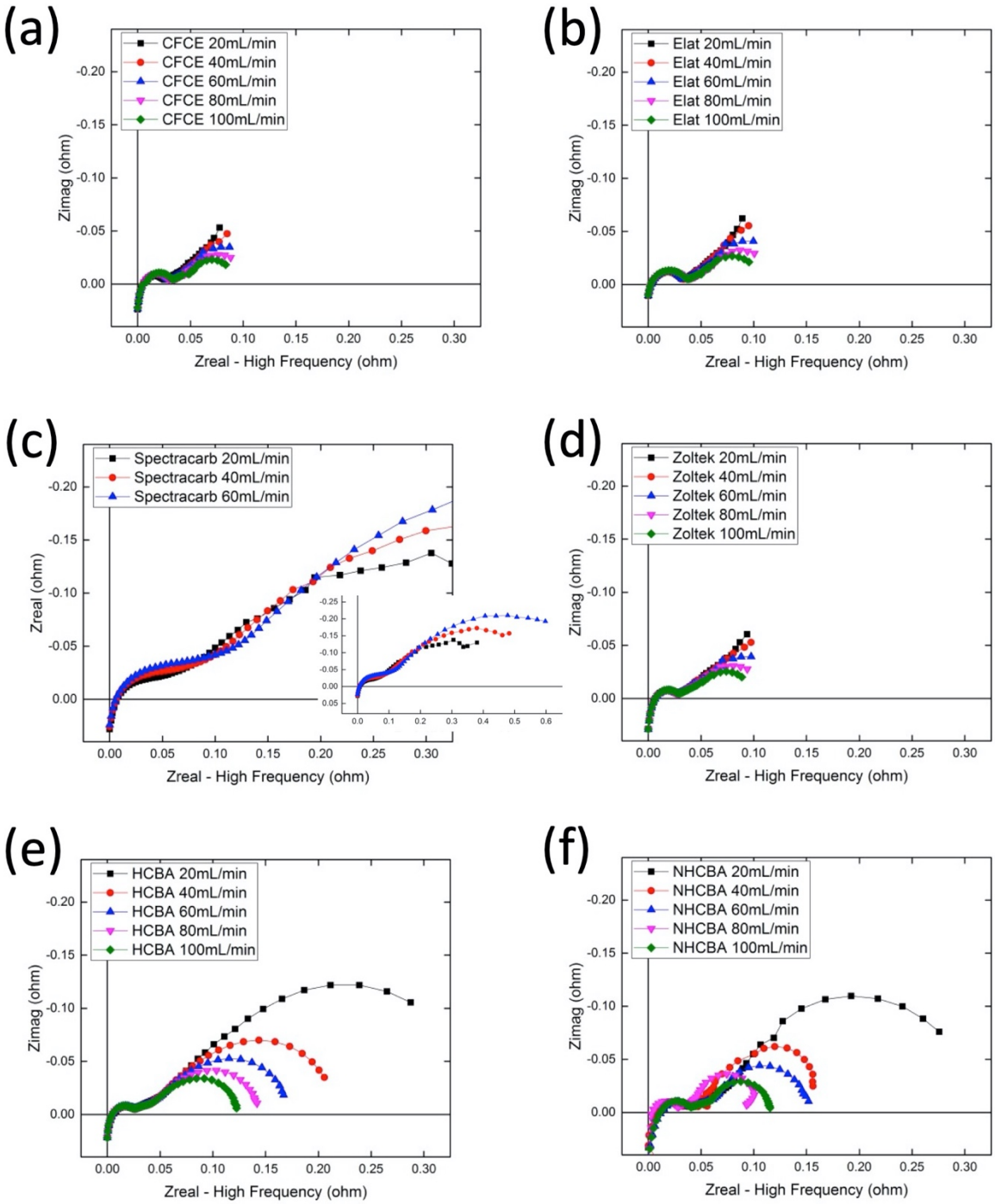

Figure S4. EIS spectra for each electrode at various volumetric flow rates. (a) CFCE), (b) Elat, (c) Spectracarb, (d) Zoltek, (e) HCBA, and (f) NHCBA graphs have all been scaled to the same axis and the high frequency resistance has been subtracted for direct comparison; the inset in (c) shows the full EIS spectrum for Spectracarb. The high frequency resistance has been subtracted from EIS spectra in (a)-(f).

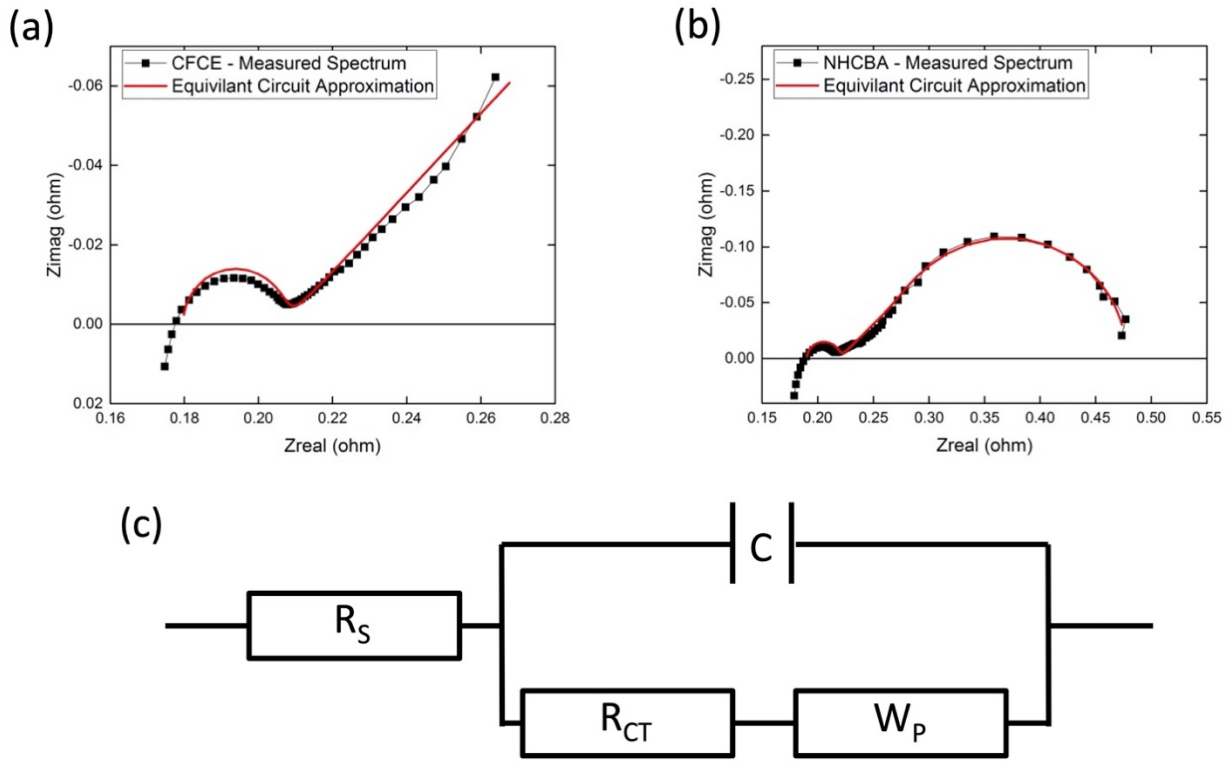

Figure S5. (a) and (b) show the EIS spectra for the CFCE and NHCBA electrodes respectively both at 20 mL/min flow. EIS spectrum (black) and a best-fit (red) for the equivalent circuit (c); R_S is the high frequency (electronic, ionic and membrane) resistance, R_{CT} is the charge transfer resistance, W_P is the semiporous Warburg impedance, and C is the double layer capacitance. R_S and R_{CT} for each EIS spectrum are tabulated in Table S2.

Table S2 gives the measured values taken at the final scan in each set of experiments, converted from R_S and R_{CT} to their area-specific quantity, ASR_S and ASR_{CT}, respectively. Note that the R_S, and therefore ASR_S, includes the membrane (Nafion 212) resistance in addition to the convoluted electronic and ionic resistance of the electrode and the electrolyte respectively.

Table S2. High-frequency (electronic, ionic and membrane: ASR_S) and charge transfer (ASR_{CT}) area-specific resistances of each electrode determined from an equivalent circuit fit to symmetric cell EIS spectra (Figure S4). The resistances from the 20 mL/min measurement are used for the simulations because they represent the most well equilibrated condition for the electrode. Areal capacitance, C, is measured at 10 kHz and approximated by the equation $C = -(\omega Z'')^{-1}$, where ω is the angular frequency ($2\pi f$) and Z'' is the imaginary impedance. Differences between BET measurements and the areal capacitance stem from the different physical properties measured by each technique [1].

Flow Rate (mL/min)	ASR (Ω cm^2)	Electrode CFCE	Elat	Spectracarb	Zoltek	HCBA	NHCBA
20	ASR_S	0.98	0.90	1.29	0.78	0.80	0.95
	ASR_{CT}	0.10	0.14	0.30	0.10	0.12	0.15
	Combined	1.08	1.04	1.59	0.88	0.92	1.10
40	ASR_S	1.09	0.98	1.37	0.80	0.82	0.97
	ASR_{CT}	0.12	0.14	0.43	0.10	0.14	0.18
	Combined	1.21	1.12	1.80	0.90	0.96	1.15
60	ASR_S	1.09	1.00	1.38	0.81	0.82	0.98
	ASR_{CT}	0.12	0.16	0.46	0.11	0.12	0.16
	Combined	1.21	1.16	1.84	0.92	0.94	1.14
80	ASR_S	1.11	1.02	-	0.83	0.82	1.04
	ASR_{CT}	0.13	0.16	-	0.11	0.12	0.20
	Combined	1.24	1.18	-	0.94	0.94	1.24
100	ASR_S	1.14	1.05	-	0.84	0.82	1.06
	ASR_{CT}	0.14	0.17	-	0.12	0.10	0.19
	Combined	1.28	1.22	-	0.96	0.92	1.25

	CFCE	Elat	Spectracarb	Zoltek	HCBA	NHCBA
Areal Capacitance with standard deviation (μF/cm^2)	340 ± 20	260 ± 10	170 ± 40	400 ± 10	420 ± 20	320 ± 20

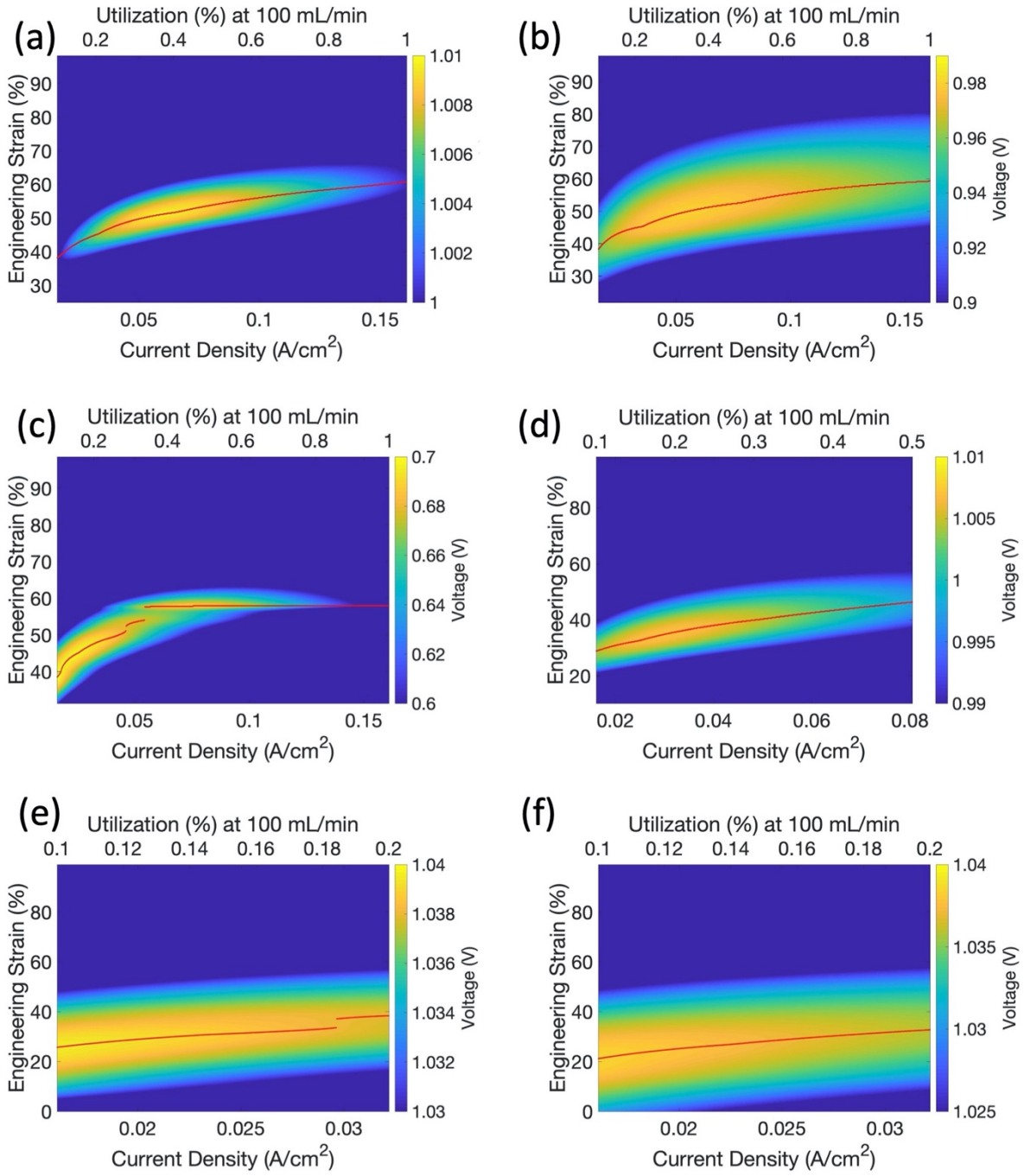

Figure S6. Global maximum operating voltage for (a) CFCE), (b) Elat, (c) Spectracarb, (d) Zoltek, (e) HCBA, and (f) NHCBA electrodes. The same parameters assumed in Figure 12 are assumed here. Note the different voltage scales and current densities used for each figure. Due to the low Ohmic resistance of the HCBA and NHCBA electrodes, the global maximum could not be resolved.

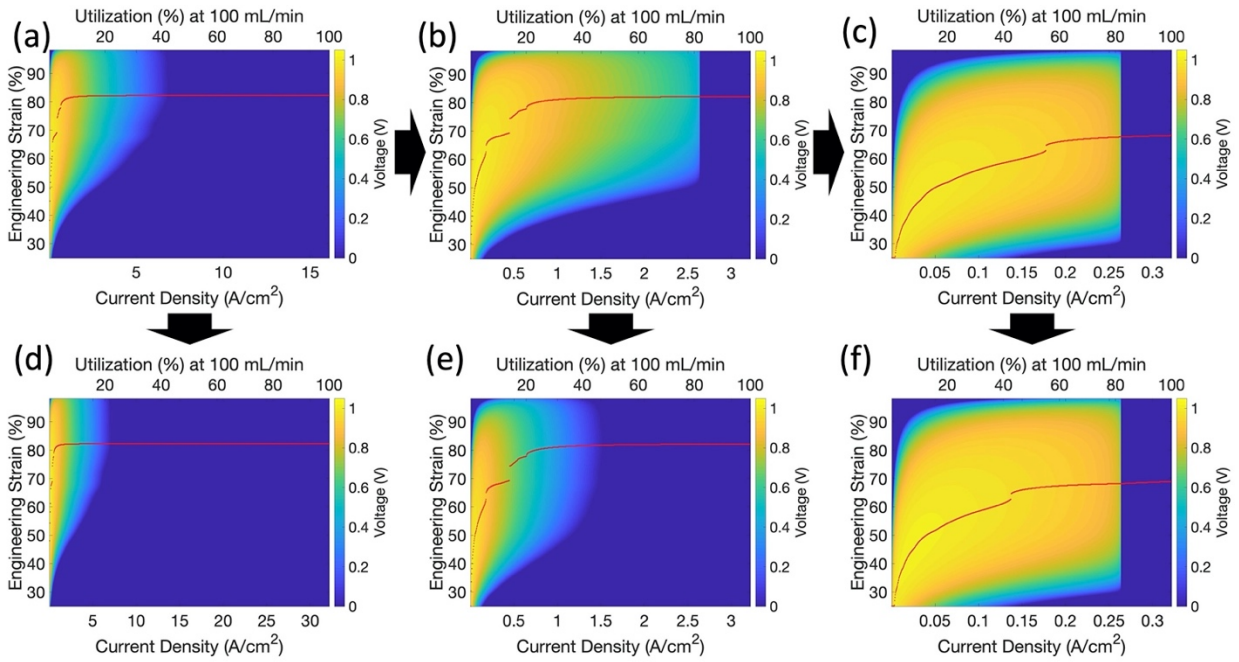

Figure S7. Calculated combined Ohmic, charge transfer, mass transfer, and pumping overvoltages as a function of strain and applied current density testing parameter sensitivity. All figures are stretched to 100% utilization. (a) Base-case using a CFCE electrode, 0.5 M one-electron electrolyte, 60% pump efficiency (S = 1.67), 100 mL/min flow rate, no membrane resistance. (b) shows the base case with 0.1 M electrolyte concentration (note the different axis scale) and (c) shows a 0.01 M electrolyte concentration, highlighting the effect of the mass transport overpotential. Pumping overvoltage losses affect the top left of the plot, at high compressions and low current densities. (d) is the base case but assuming a two electron reduction process (n = 2). (e) is the same condition as depicted in (b) with a 0.1 M electrolyte concentration, except including a 0.5 Ωcm^2 membrane resistance. It is very evident that even a low membrane resistance has a profound impact on the overvoltage but does not change the optimum strain (red dot) as this property is independent of electrode thickness. (f) is the same 0.01 M electrolyte condition as (c) case but with a 100% pumping efficiency (S = 1), indicating that at only at low concentrations, low current densities, and high compressions are pumping losses impactful.

To understand the sensitivity to some of the assumed parameters, Figure S7 details the effects of pump efficiency, concentration (a proxy for SOC), and membrane resistance. All figures show 0%-100% utilization. Figure S7(a) represents the base case of 0.5 M $K_4Fe(CN)_6$ with a 60% pump efficiency, and no membrane resistance. Figure S7(b) and (c) use a 0.1M and 0.01M $K_4Fe(CN)_6$ concentration respectively, depicting how mass transport effects begin to dominate at lower current densities due to the higher electrolyte utilization. The ideal strain value also decreases, due to the higher impact of pumping losses. Figure S7(d) uses the same parameters as (a) except for a 100% pump efficiency. Under these high concentration operating conditions, pumping has a negligible effect on the optimum efficiency. In contrast though, the addition of membrane resistance has a profound impact on the overvoltage as seen in Figure S7(e), which is identical to (b) except for the addition of a 0.5 Ωcm^2 resistance. Though this effect has no impact on the optimum electrode

thickness, membrane resistance significantly lowers the voltage efficiency, and therefore overall energy efficiency of the RFB.

Table S3. Comparison of electrolyte volumes and compositions, and full cell performance between this work and experiments published by Kwabi *et al.* [2]

Electrolyte	This Work	Kwabi *et al.* [2]
Negolyte	6 mL 0.5 M DBEAQ 0.01 M KOH	5 mL 0.5 M DBEAQ 0.01 M KOH
Posolyte	15 mL 0.5 M $K_4Fe(CN)_6$ 0.05 M $K_3Fe(CN)_6$ 0.01 M KOH	38 mL 0.3 M $K_4Fe(CN)_6$ 0.1 M $K_3Fe(CN)_6$ 0.01 M KOH
Open Circuit Voltage at ~100% SOC	CFCE: 1.31 V Elat: 1.25 V Zoltek: 1.28 V	1.12 V
DC-ASR at ~100% SOC	CFCE: 0.86 Ωcm^2 Elat: 0.86 Ωcm^2 Zoltek: 0.92 Ωcm^2	1.47 Ωcm^2

Under non-mass transport limited regimes with losses dominated by DC-ASR, r, the power density, p, can be approximated as

$$p = (V_{oc} - ir)i \tag{1}$$

where V_{oc} is the open circuit voltage. Therefore, the peak power density, p_p, can be approximated as

$$p_p = \frac{{V_{oc}}^2}{4r} \tag{2}$$

From this relationship, we can determine the relative increases to peak power density as a function of electrolyte modification, through an increase in ${V_{oc}}^2$, and as a function of electrode engineering through a reduction in r. The V_{oc} attained at ~100% SOC in this work is ~1.30 V compared to 1.12 V from Kwabi *et al*. (see Table S3), leading to a ratio of 1.69 V^2 : 1.25 V^2. Therefore, an approximately 35% increase in peak power density is attributable to enhancements from the electrolyte composition. In contrast, the DC-ASR attained at ~100% SOC in this work is ~0.90 Ωcm^2 compared to 1.47 Ωcm^2 from Kwabi *et al*. suggesting that an over 60% increase in peak power density is attributable to improved cell engineering.

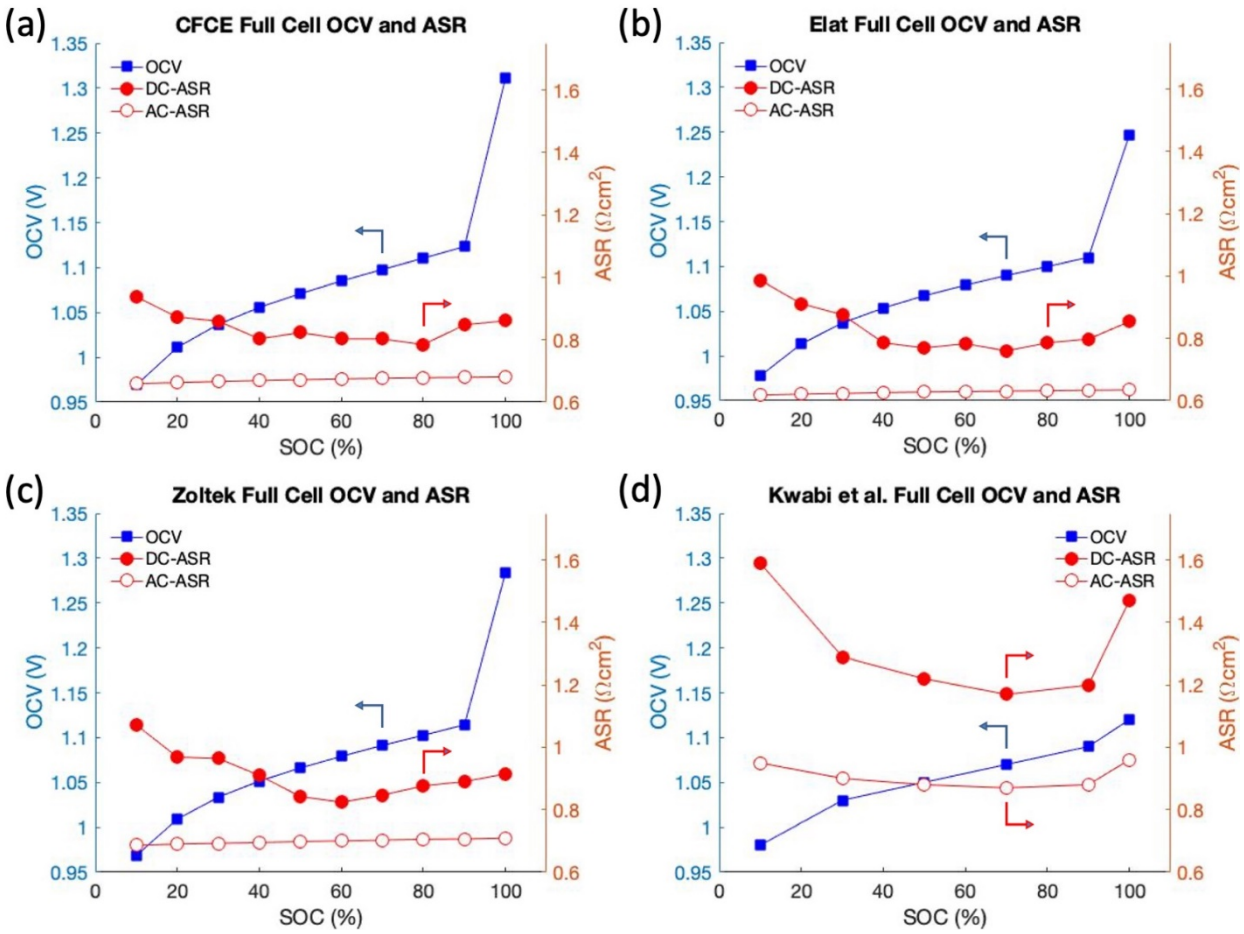

Figure S8. Comparison of full cell AC- and DC-ASR and OCV as a function of SOC for this work and Kwabi *et al*. [2]. Specific electrolyte compositions are described in Table S3. Relatively similar OCV values persist between the two works below 100% SOC. In contrast, AC- and DC-ASR are systematically lower by about 30%.

Below ~100% SOC however, Figure S8 indicates that the OCV between this work and Kwabi *et al*. are remarkably consistent. In contrast, the DC-ASR is about 30% lower across a wide range of SOCs, suggesting an approximately 50% increase in peak power when under non-mass transport limited conditions. This further strengthens the case that the full cell performance reported in this work is enhanced primarily by a thoughtful application of these porous electrodes.

References:

[1] S. Trasatti and O. A. Petrii, "Real Surface Area Measurements in Electrochemistry," *Journal of Electroanalytical Chemistry,* 327, 353-376 (1992).

[2] D. Kwabi, K. Lin, Y. Ji, E. Kerr, M.-A. Goulet, D. De Porcellinis, D. Tabor, D. A.-G. A. Pollack, R. Gordon and M. Aziz, "Alkaline quinone flow battery with long lifetime at pH 12," *Joule,* 2, 1907 (2018).

List of Variables:

ASR_S	high frequency (electronic, ionic and membrane) area specific resistance [Ωcm^2]
C	double layer capacitance [F]
p	power density [W/cm^2]
p_p	peak power density [W/cm^2]
R_S	high frequency (electronic, ionic and membrane) resistance [Ω]
R_{CT}	charge transfer resistance [Ω]
r	DC area specific resistance [Ωcm^2]
V_{oc}	open circuit voltage [V]
W_P	semiporous Warburg impedance [Ω]